Supporting information

Thick-Layer Lead Iodide Perovskites with Bifunctional Organic Spacers Allylammonium and Iodopropylammonium Exhibiting Trap-State Emission

Eugenia S. Vasileiadou, [1] Xinyi Jiang, [1] Mikaël Kepenekian,[2] Jacky Even, [3] Michael C. De Siena,[1] Vladislav Klepov, [1] Daniel Friedrich, [1] Ioannis Spanopoulos, [1#] Qing Tu,[4] Imra S. Tajuddin, [1] Emily A. Weiss [1] and Mercouri G. Kanatzidis [1,*]

[1] *Department of Chemistry, Northwestern University, Evanston, IL 60208, United States.*

[2] *Univ Rennes, ENSCR, CNRS, ISCR − UMR 6226, F-35000 Rennes, France.*

[3] *Univ Rennes, INSA Rennes, CNRS, Institut FOTON − UMR 6082, F-35000 Rennes, France.*

[4] *Department of Materials Science & Engineering, Texas A&M University, College Station, Texas 77840, United States*

Table of contents

1. Methods

XRD measurements

Single-crystal X-ray diffraction

Single crystal diffraction experiments were performed
(1) Using a four-circle Rigaku XtaLAB Synergy system equipped with a PhotonJet (Mo, λ= 0.71073 Å) micro-focus sealed X-ray tube and Hybrid Pixel Array Detector at 273 K, 293 K and 323 K.
(2) Using either a Bruker Molly or Duo instrument with MoKα IμS microfocus source (λ= 0.71073 Å) with MX Optics at 293 K.
(3) Using either a STOE IPDS 2 or an IPDS 2T diffractometer with graphite-monochromatized Mo Kα radiation (λ = 0.71073 Å) (50 kV/40 mA) 293 K.
The collected data were integrated and applied with multiscan absorption correction using the APEX3 or STOE X-AREA software. The structure was solved by charge flipping and refined by full-matrix least squares on F^2 with the Jana2006 package. [1]

Powder X-ray diffraction

Powder X-ray diffraction patterns were collected on a Rigaku Miniflex system (CuKα radiation) operated at 40 kV and 15 mA. A typical scan rate was 15 sec/step with a step size of 0.02 deg.

Optical Absorption Spectroscopy:

Optical diffuse reflectance measurements were performed using a Shimadzu UV-3600 UV−VIS NIR spectrometer operating in the 200−2500 nm region at room temperature. $BaSO_4$ was used as a non-absorbing reflectance reference for all measurements. The bandgap was estimated by diffuse reflectance spectroscopy on powder samples of the studied materials, where the Kubelka-Munk model was used to derive absorption values.[2]

Steady-State Photoluminescence:

The samples were excited at 405 nm with an optical parametric amplifier, which was pumped by a Ti:sapphire amplifier (Spectra-Physics) with 800-nm output at 5-MHz repetition rate.

SEM studies:

Scanning Electron Microscopy (SEM) measurements were recorded on EPIC SEM Hitachi S-3400.

Density Functional Theory Calculations (DFT):

First-principles calculations are based on density functional theory (DFT) as implemented in the SIESTA package [3,4] The nonlocal van der Waals density functional of Dion *et al.* corrected by Cooper (C09) is used for geometry optimizations. [5-6] Spin-orbit coupling is taken into account through the fully relativistic pseudopotential approach. [7] To prevent conflicts between the spin-orbit coupling treatment and the nonlocality of C09 functional, single point calculations are conducted with the revPBE functional on which C09 is based. [8] Core electrons are described with Troullier-Martins pseudopotentials [9], while valence wavefunctions are developed over double-ζ polarized basis set of finite-range numerical pseudoatomic orbitals.[10] In all cases, an energy cutoff of 150 Ry for real-space mesh size has been used. Experimental structures are used for the inorganic skeleton, well characterized by X-ray diffraction. On the other hand, the positions of light atoms, more difficult to grasp experimentally, are optimized. In addition, we provide high-frequency dielectric constant profiles along the stacking direction following the recipe detailed thoroughly in previous studies. [11-12]

Transient Absorption Microscopy:

The fundamental 1030-nm beam was generated from an Yb:KGW amplifier system (Light Conversion, Pharos) operating at 200 kHz with a pulse duration of 190 fs. The fundamental beam was split into pump and probe arms. The tunable pump was generated using a collinear optical parametric amplifier (OPA, 200 – 3000 nm, Light Conversion, Orpheus) and then delayed compared to the probe with a high resolution motorized linear stage (Newport). The pump was modulated at the frequency of 2 kHz by a mechanical chopper (New Focus, Newport). The chopper was synced to the camera using the same clocking source generated by the Pharos laser. The white-light probe (550–750 nm) was generated by focusing the fundamental beam into an yttrium aluminum garnet (YAG) crystal. Both beams were recombined and focused collinearly onto the sample with a 74× reflective objective (NA 0.65, Beck). The beam spot size of 0.6 μm was determined by measuring the power passing through a pinhole and then calculated using a

Gaussian beam profile. The sample was clamped on a piezo-driven XYZ stage with a resolution of 0.2 μm (nanoPI, Physik Instrumente). The signal was collected using a 100× refractive objective (NA 0.70, Mitutoyo), spatially filtered through a 150-μm pinhole, and then spectrally dispersed in a spectrometer (Shamrock). The TA signal was detected using a high-speed CMOS camera (Andor, Zyla 4.2). The system was controlled using custom LabVIEW program. Linear absorption and photoluminescence (PL) maps were measured within the same setup.

Nanoindentation:

Hardness and indentation modulus were measured using a Hysitron 950 Triboindenter with a Berkovich indenter (three-sided pyramid shape diamond tip, tip radius ~ 100 nm) in ambient environment. Large single crystal flakes of 2D perovskites were first mounted onto stainless steel atomic force microscopy specimen discs by epoxy (J-B Kwik) with the (001) plane facing up. The indentation is along the stacking axis of the crystals, enabled by their 2D flake nature. Prior to nanoindentation, the top few layers were mechanically exfoliated by scotch tape to remove any potential surface contamination/degradation and reveal fresh crystal plane.

For all measurements, the loading and unloading were kept at about 70 μN/s and before unloading the indenter was hold at constant load for 30s. The peak load was kept at 1000 μN for samples with different n number while for samples with different spacer molecules, the peak load was kept at 500 μN so that the indentation depth can be kept within 500 nm. These experimental parameters are kept the same as those in our earlier studies to facilitate the direct comparison of the values.[13-14] The data were analyzed using standard Oliver and Pharr analysis to extract reduced moduli and hardness.[15-16] The elastic modulus E of the materials can be further derived with a Young's modulus E of 1141 GPa and Poisson's Ratio ν of 0.07 for diamond tip[16] and ν = 0.3 for 2D perovskites.[14, 17-18] More than 3 crystals were checked for each type of samples. 10 to 20 indentations were performed on each crystal and the reported values for each type of samples were averaged by these measurements.

2. Complementary Syntheses

Non-Perovskite Structures with Allylamine Spacer Cation

$(AA)_3Pb_2I_7$

PbO (1 mmol; 223 mg) powder was dissolved in a mixture of 2 mL HI and 0.25 mL hypophosphorous acid (H_3PO_2) by heating to boiling under constant magnetic stirring, until a clear yellow solution was obtained. The reaction solution was left on the hotplate to cool to room temperature, under continuing stirring. Next, AA^+Cl^- salt (1.5 mmol; 140 mg) was added to the reaction solution at room temperature (R.T.), under continuous stirring. The stirring was discontinued after 10 minutes and the reaction solution was transferred to a petri dish for slow evaporation. Yellow needle-like crystals precipitated from the reaction vial. The crystals were isolated by vacuum filtration and dried under vacuum overnight. Yield : 67 mg, 9.07 % based on total Pb.

$(AA)_{12}(MA)_2Pb_9I_{32}$

PbO (2 mmol; 446 mg) and MACl (1 mmol; 70 mg) powders were dissolved in a mixture of 2 mL HI and 0.25 mL hypophosphorous acid (H_3PO_2) by heating to boiling under constant magnetic stirring, until a clear yellow solution was obtained. The reaction solution was left on the hotplate to cool to room temperature, under continuing stirring. Next, AA^+Cl^- salt (2 mmol; 187 mg) was added to the reaction solution at room temperature (R.T.), under continuous stirring. The stirring was discontinued after 10 minutes and the reaction solution was transferred to a petri dish for slow evaporation. Orange crystals co-precipitated from the petri dish, along with yellow crystals of $(AA)_3Pb_2I_7$.

<u>Non-Perovskite Structures with Iodopropylamine Spacer Cation</u>

$(IdPA)PbI_3$

PbO (1 mmol; 223 mg) powder was dissolved in a mixture of 2 mL HI and 0.25 mL hypophosphorous acid (H_3PO_2) by heating to boiling under constant magnetic stirring, until a clear yellow solution was obtained. Next, $IdPA^+I^-$ salt (1 mmol; 187 mg) was added to the reaction solution, under continuous stirring and heating. The stirring was discontinued after 5 minutes and the reaction solution was left on the hotplate to cool to room temperature. Yellow needle-like crystals precipitated from the reaction solution. The crystals were isolated by vacuum filtration and dried under vacuum overnight. Yield : 54 mg, 8.35 % based on total Pb.

$(IdPA)_6Pb_3I_{12} = (IdPA)_2PbI_4$

PbO (1 mmol; 223 mg) powder was dissolved in a mixture of 2 mL HI and 0.25 mL hypophosphorous acid (H_3PO_2) by heating to boiling under constant magnetic stirring, until a clear yellow solution was obtained. Next, $IdPA^+I^-$ salt (2 mmol; 372 mg) was added to the reaction solution, under continuous stirring and heating. The stirring was discontinued after 5 minutes and the reaction solution was left on the hotplate to cool to room temperature. Yellow rod-like crystals precipitated from the reaction solution. The crystals were isolated by vacuum filtration and dried under vacuum overnight. Yield : 179 mg, 16.47 % based on total Pb.

3. Additional structural and characterization data

3.1 Nanoindentation Data

Table S1. Average Elastic Modulus (*E*) and Hardness (*H*) of $(AA)_2MA_2Pb_3I_{10}$, $(BA)_2MA_2Pb_3I_{10}$, and Diammonium $(NH_3C_8H_{16}NH_3)MA_2Pb_3I_{10}$ Crystals. The values in the parenthesis indicates the standard deviation of the measured values.

	$(AA)_2MA_2Pb_3I_{10}$	$(BA)_2MA_2Pb_3I_{10}$	$(NH_3C_8H_{16}NH_3)MA_2Pb_3I_{10}$
E (GPa)	5.74 (0.48)	4.40 (0.57)	11.65 (1.76)
H (GPa)	0.430 (0.066)	0.426 (0.072)	0.828 (0.235)

3.2 Single Crystal X-ray Diffraction

Table S2. Crystal Data and Structure Refinement for $[(AA)_x(IPA)_{1-x}]_2MA_{n-1}Pb_nI_{3n+1}$ (*n*=1-3).

	$[(AA)_x(IdPA)_{1-x}]_2PbI_4$ (*n*=1)	$[(AA)_x(IdPA)_{1-x}]_2(MA)Pb_2I_7$ (*n*=2)	$[(AA)_x(IdPA)_{1-x}]_2(MA)_2Pb_3I_{10}$ (*n*=3)
Crystal system	orthorhombic	monoclinic	monoclinic
Space group	$P2_1/c$	Cc	$P2_1/c$
Crystal Shape	Yellow Plate	Bright Red Plate	Dark Red Plate
Unit cell dimensions (Å)	a = 12.659	a = 39.192(7)	a = 26.439(5) Å
	b = 8.685	b = 8.8278(11)	b = 8.8658(18) Å
	c = 8.757	c = 8.8418(13)	c = 8.8738(18) Å
	β = 110.11°	β = 90.283(13)°	β = 99.59(3)°
Volume ($Å^3$)	904.0	3059.0 (8)	2050.9(7)
Z	1	4	2
Density (calculated, g/cm^3)	3.053	3.1462	3.308
Independent reflections	1741 [R_{int} = 0.0894]	2650 [R_{int} = 0.0813]	4022 [R_{int} = 0.2645]
Completeness to θ = 25.350°/ 29.27°/29.24/	98.9%	96%	99.5%
Data / restraints / parameters	1741 / 3 / 43	2650 / 11 / 131	4022 / 9 / 81
Goodness-of-fit	1.006	3.34	1.260
Final R indices [I>3σ(I)]	R_{obs} = 0.0729, wR_{obs} = 0.1894	R_{obs} = 0.0844, wR_{obs} = 0.1978	R_{obs} = 0.1371, wR_{obs} = 0.3569

R indices [all data]	R_{all} = 0.0843, wR_{all} = 0.2000	R_{all} 0.1683, wR_{all} = 0.2127	R_{all} = 0.1602, wR_{all} = 0.3884

R = Σ||Fo|-|Fc|| / Σ|Fo|, wR = {Σ[w(|Fo|2 - |Fc|2)2] / Σ[w(|Fo|4)]}1/2 and w=1/(σ2(I)+0.0004I2)

Table S3. Crystal Data and Structure Refinement for $(IdPA)_6Pb_3I_{12}$ and $(IdPA)PbI_3$.

	$(IdPA)_6Pb_3I_{12}$	$(IdPA)PbI_3$
Empirical formula	$C_{18}H_{54}N_6Pb_3I_{18}$	$C_3H_9NPbI_4$
Crystal system	triclinic	monoclinic
Space group	$P\bar{1}$	$P2_1/c$
Crystal Shape	Yellow rod	Light Yellow Needle
Unit cell dimensions (Å)	a = 13.8784(2) Å,	a = 4.7089(9)
	b = 15.7077(4) Å	b = 13.499(3)
	c = 16.1226(3) Å	c = 21.998(4)
	α = 98.718(2)° β = 100.907(2)° γ = 114.490(2)°	β = 91.46(3)°
Volume ($Å^3$)	3034.88(12)	1397.8(5)
Z	2	4
Density (calculated, g/cm^3)	3.508	3.677
Independent reflections	17599 [R_{int} = 0.0478]	2749 [R_{int} = 0.0771]
Completeness to θ = 25.242°	99.9%	99.9 %
Data / restraints / parameters	17599 / 45 / 259	2749 / 9 / 61
Goodness-of-fit	1.174	1.075
Final R indices [I>3σ(I)]	R_{obs} = 0.0841, wR_{obs} = 0.3035	R_{obs} = 0.0720, wR_{obs} = 0.2131
R indices [all data]	R_{all} = 0.1275, wR_{all} = 0.3308	R_{all} = 0.0926, wR_{all} = 0.2197

R = Σ||Fo|-|Fc|| / Σ|Fo|, wR = {Σ[w(|Fo|2 - |Fc|2)2] / Σ[w(|Fo|4)]}1/2 and w=1/(σ2(I)+0.0004I2)

3.3 Powder X-ray Diffraction Measurements

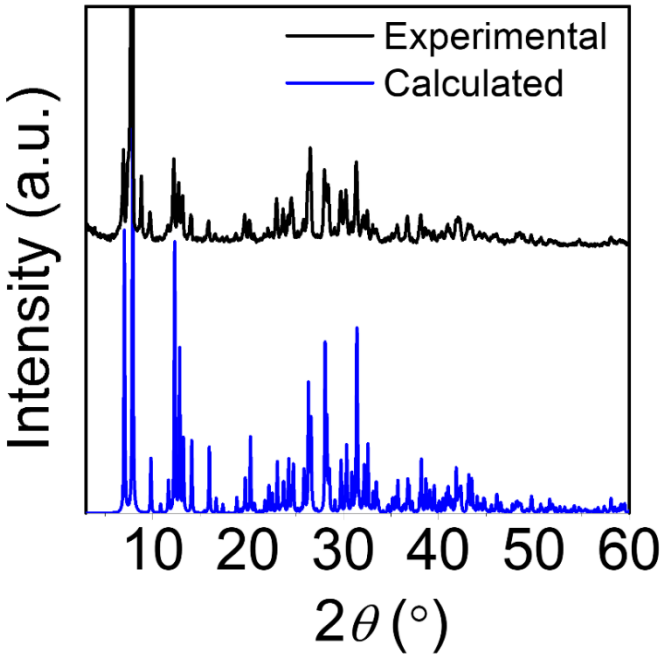

Figure S1. Comparison of the experimental PXRD pattern from crystals with the calculated PXRD pattern from the solved single crystal structure of $(AA)_3Pb_2I_7$ from in-house instrument (λ = 1.5406 Å).

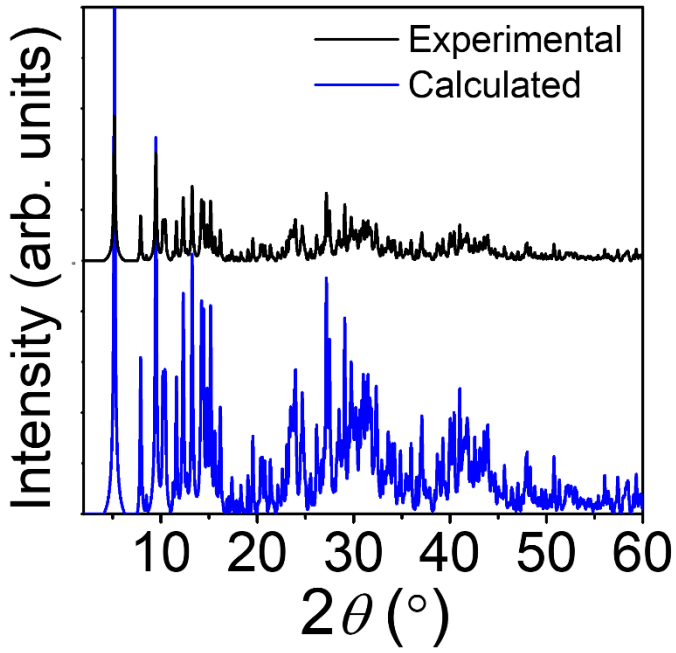

Figure S2. Comparison of the experimental PXRD pattern from crystals with the calculated PXRD pattern from the solved single crystal structure of $(AA)_{12}(MA)_2Pb_9I_{32}$ (m=4) from in-house instrument (λ = 1.5406 Å).

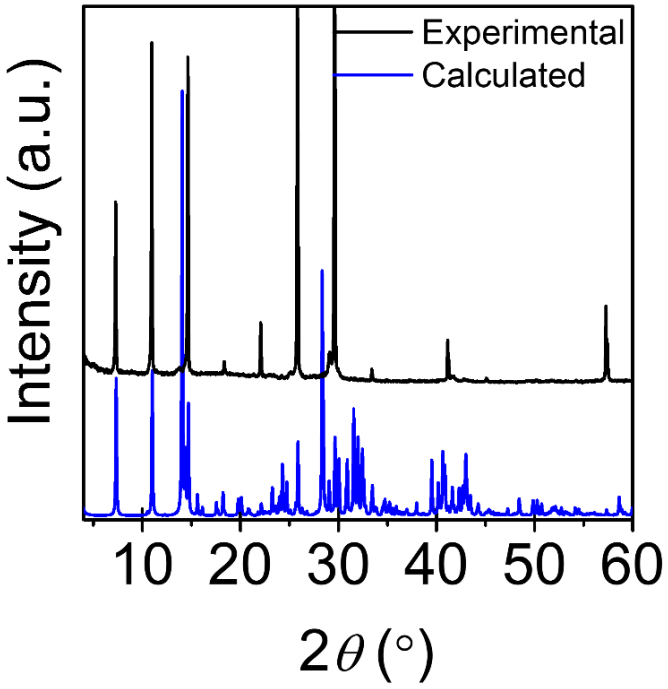

Figure S3. Comparison of the experimental PXRD pattern from crystals with the calculated PXRD pattern from the solved single crystal structure of $(AA)_2(MA)_2Pb_3I_{10}$ (n=3) from in-house instrument (λ = 1.5406 Å).

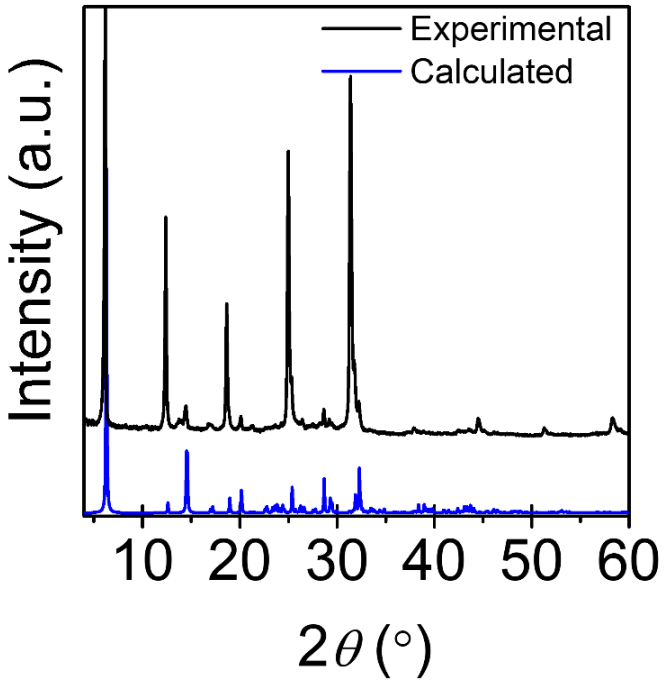

Figure S4. Comparison of the experimental PXRD pattern from crystals with the calculated PXRD pattern from the solved single crystal structure of $(IdPA)_2PbI_4$ (n =1) from in-house instrument (λ = 1.5406 Å).

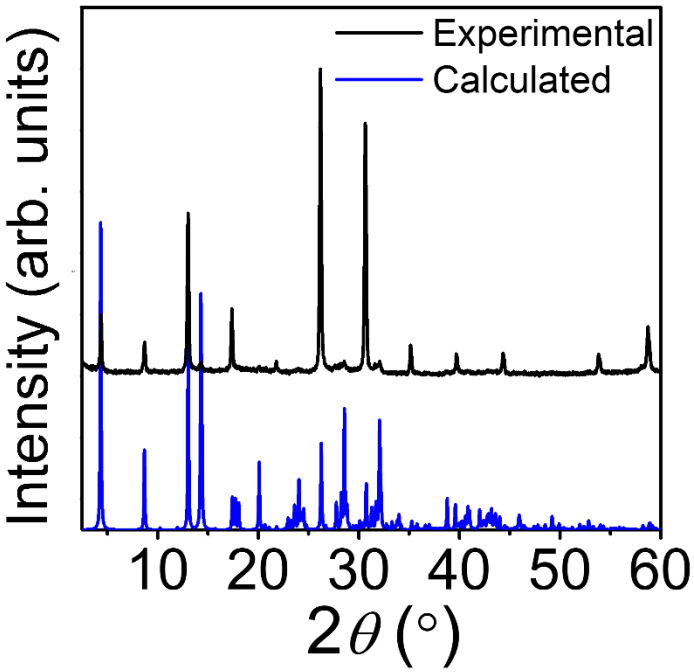

Figure S5. Comparison of the experimental PXRD pattern from crystals with the calculated PXRD pattern from the solved single crystal structure of $(IdPA)_2(MA)Pb_2I_7$ (n =2) from in-house instrument (λ = 1.5406 Å).

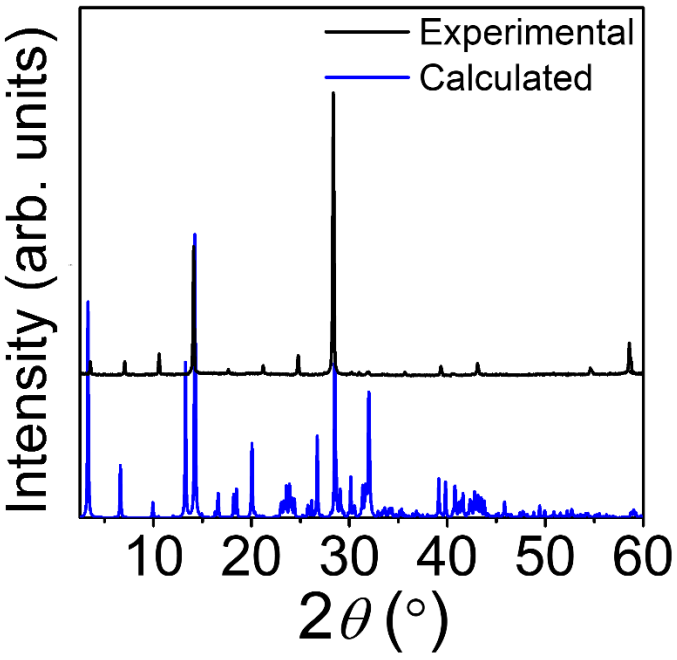

Figure S6. Comparison of the experimental PXRD pattern from crystals with the calculated PXRD pattern from the solved single crystal structure of $(IdPA)_2(MA)_2Pb_3I_{10}$ (n=3) from in-house instrument (λ = 1.5406 Å).

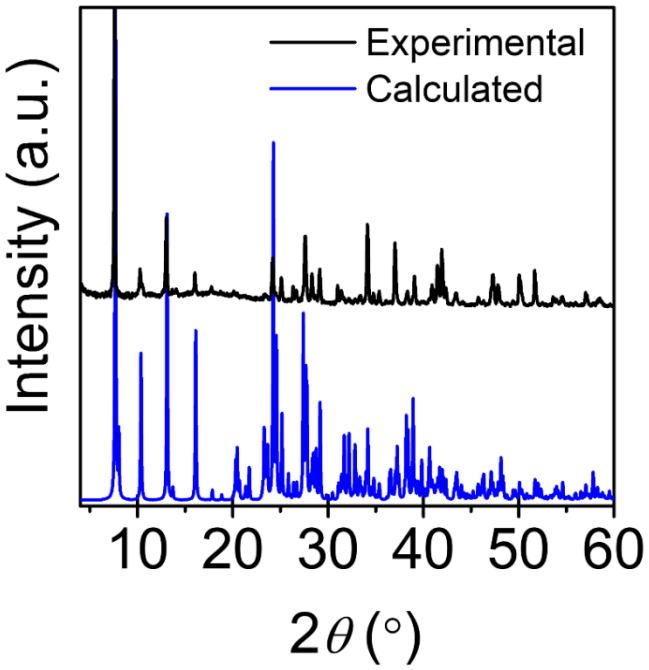

Figure S7. Comparison of the experimental PXRD pattern from crystals with the calculated PXRD pattern from the solved single crystal structure of (IdPA)PbI_3 from in-house instrument (λ = 1.5406 Å).

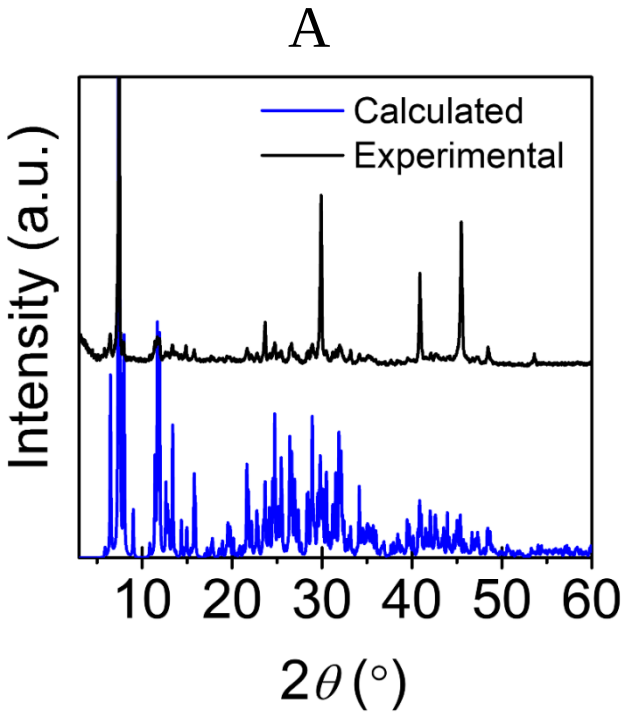

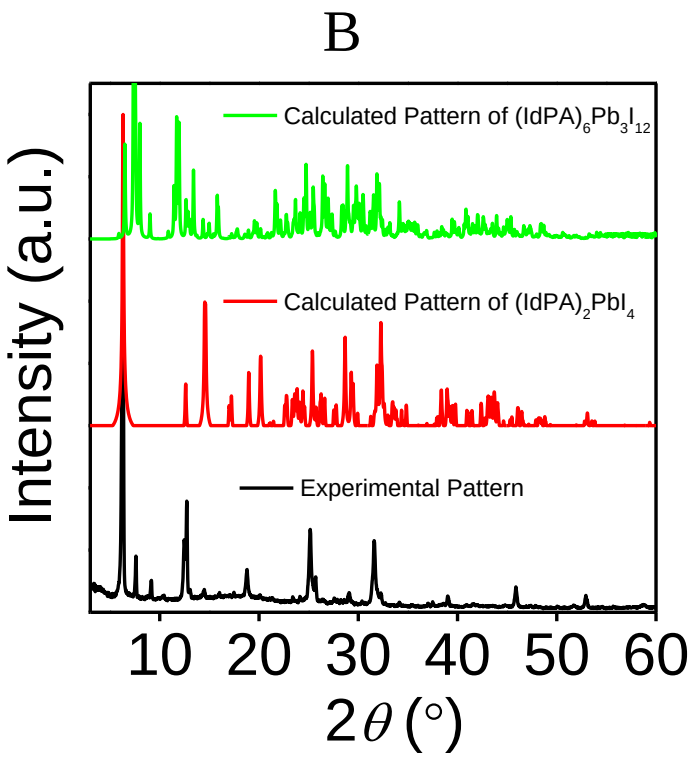

Figure S8. (A) Comparison of the experimental PXRD pattern from $(IPA)_6Pb_3I_{12}$ crystals with the calculated PXRD pattern from the solved single crystal structure of $(IdPA)_6Pb_3I_{12}$ from in-house instrument (λ = 1.5406 Å). **(B)** Experimental PXRD pattern from a sample of targeted synthesis $(IdPA)_2PbI_4$ (n =1) collected the next day containing both phases of $(IdPA)_2PbI_4$ (n =1) and 0D $(IdPA)_6Pb_3I_{12}$, in compairson to calculated PXRD pattern from the solved single crystal structure of $(IdPA)_6Pb_3I_{12}$ and $(IdPA)_2PbI_4$ (n =1).

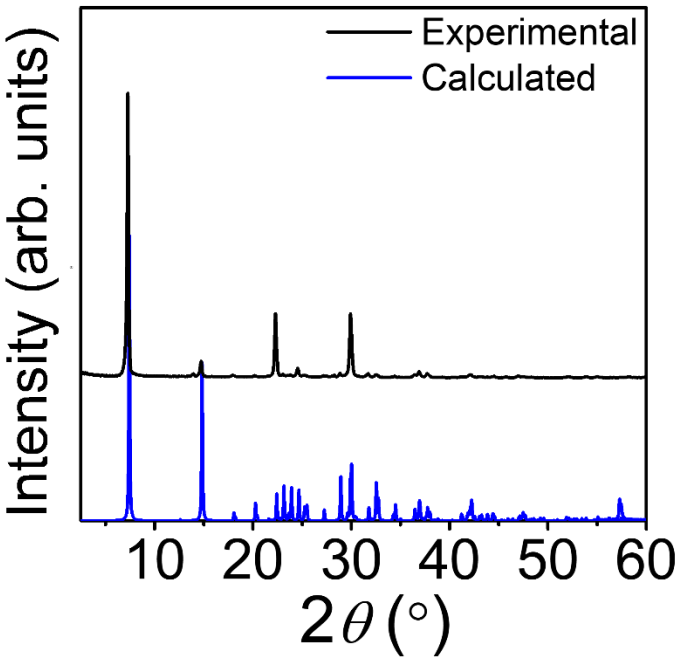

Figure S9. Comparison of the experimental PXRD pattern from crystals with the calculated PXRD pattern from the solved single crystal structure of $[(AA)_x(IdPA)_{1-x}]_2PbI_4$ (n=1) from in-house instrument (λ = 1.5406 Å).

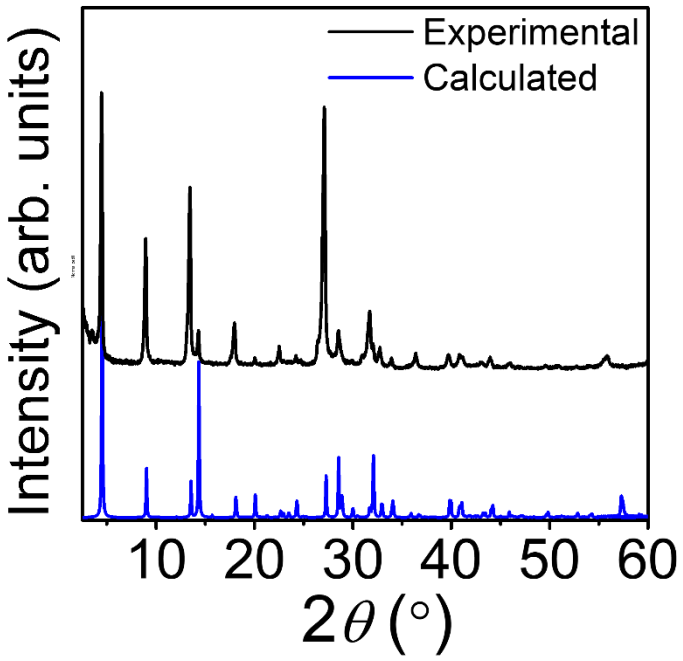

Figure S10. Comparison of the experimental PXRD pattern from crystals with the calculated PXRD pattern from the solved single crystal structure of $[(AA)_x(IdPA)_{1-x}]_2(MA)Pb_2I_7$ (n=2) from in-house instrument (λ = 1.5406 Å).

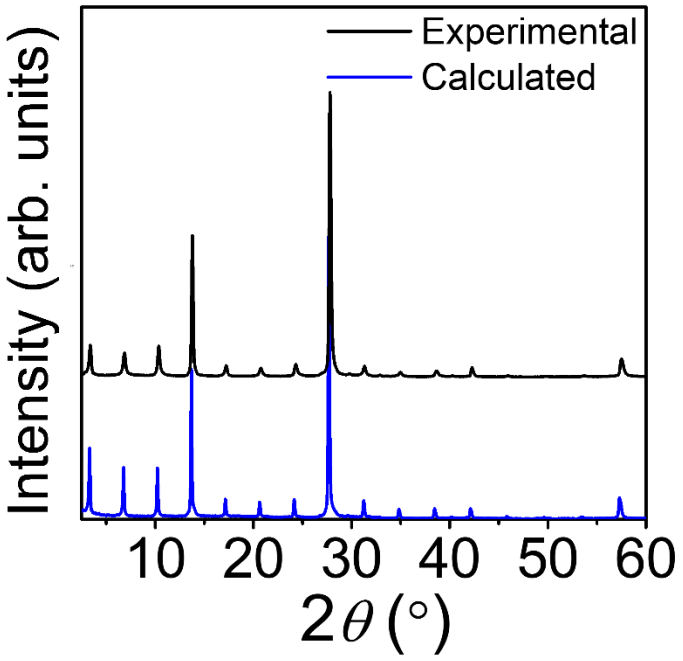

Figure S11. Comparison of the experimental PXRD pattern from crystals with the calculated PXRD pattern from the solved single crystal structure of $[(AA)_x(IdPA)_{1-x}]_2(MA)_2Pb_3I_{10}$ (n=3) from in-house instrument (λ = 1.5406 Å).

3.4 Electronic Structure Calculations and Dielectric Properties

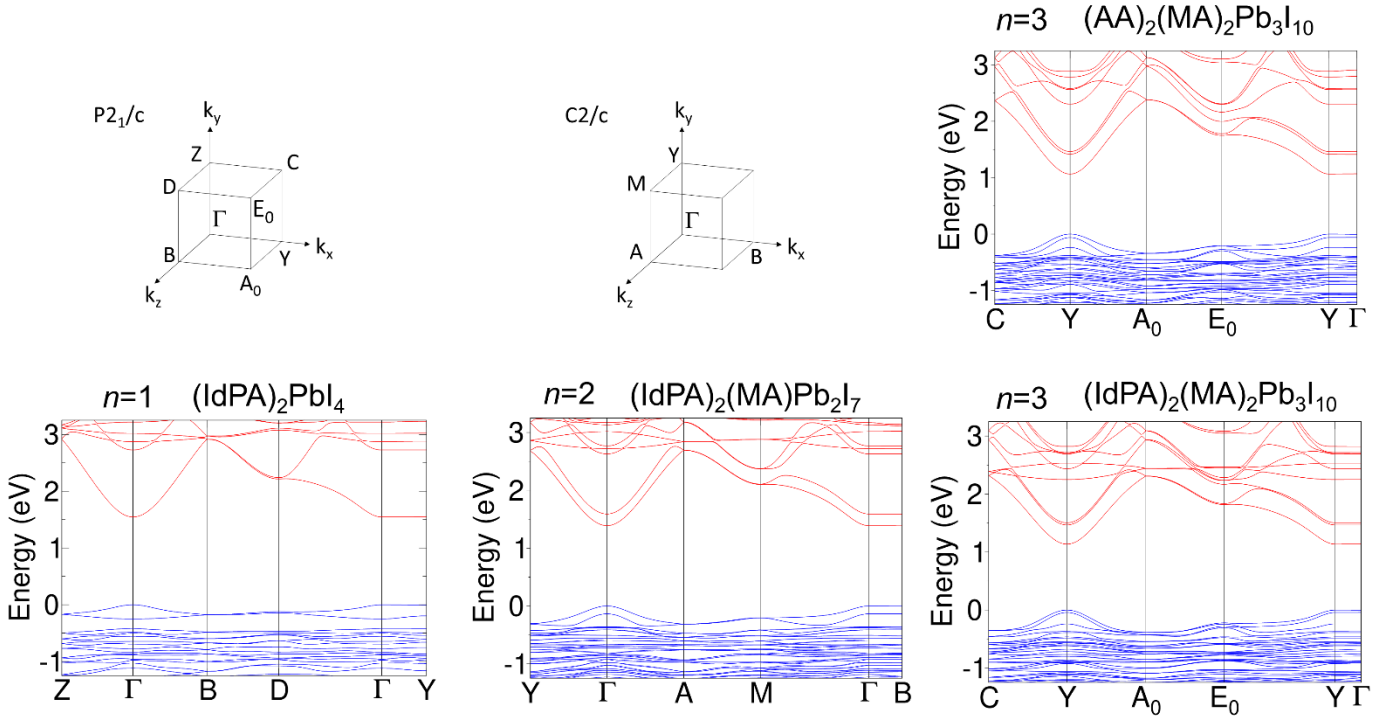

Figure S12. Computed band structures for the $(IdPA)_2(MA)_{n-1}Pb_nI_{n+1}$ (n=1-3) series and the n=3 $(AA)_2(MA)_2Pb_3I_{10}$ compound. The Brillouin zone for $P2_1/c$ ($(IdPA)_2PbI_4$, $(IdPA)_2(MA)_2Pb_3I_{10}$, and $(AA)_2(MA)_2Pb_3I_{10}$) and $C2/c$ ($(IdPA)_2(MA)Pb_2I_7$) are given. All band structures present similar features with direct band gaps and important dispersions perpendicular to the stacking axis. For the $(IdPA)_2(MA)_{n-1}Pb_nI_{n+1}$ (n=1-3) series, we observe the closing of the bandgap for increasing values of n, which marks the decreasing of the quantum confinement. $(IdPA)_2(MA)_2Pb_3I_{10}$ and $(AA)_2(MA)_2Pb_3I_{10}$ band structures are very similar, underlying the small electronic influence of cation near the band gap.

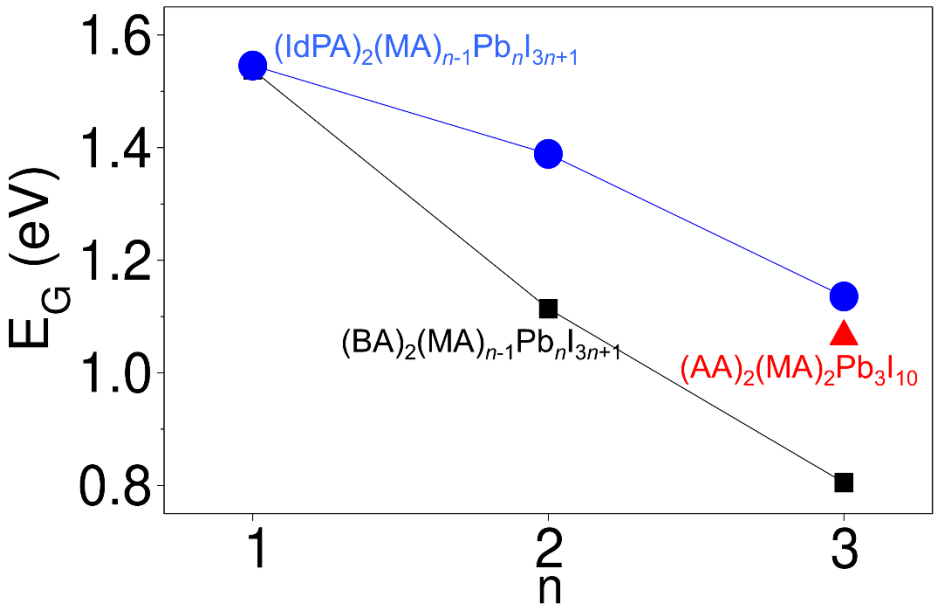

Figure S13. Computed band gaps for the $(IdPA)_2(MA)_{n-1}Pb_nI_{n+1}$ (n=1-3) series (blue circles), $(AA)_2(MA)_2Pb_3I_{10}$ (red triangle) and the $(BA)_2(MA)_{n-1}Pb_nI_{n+1}$ (n=1-3) series (black squares). The well-known $(BA)_2(MA)_{n-1}Pb_nI_{n+1}$ series are archetypical structures of layered halide perovskites.

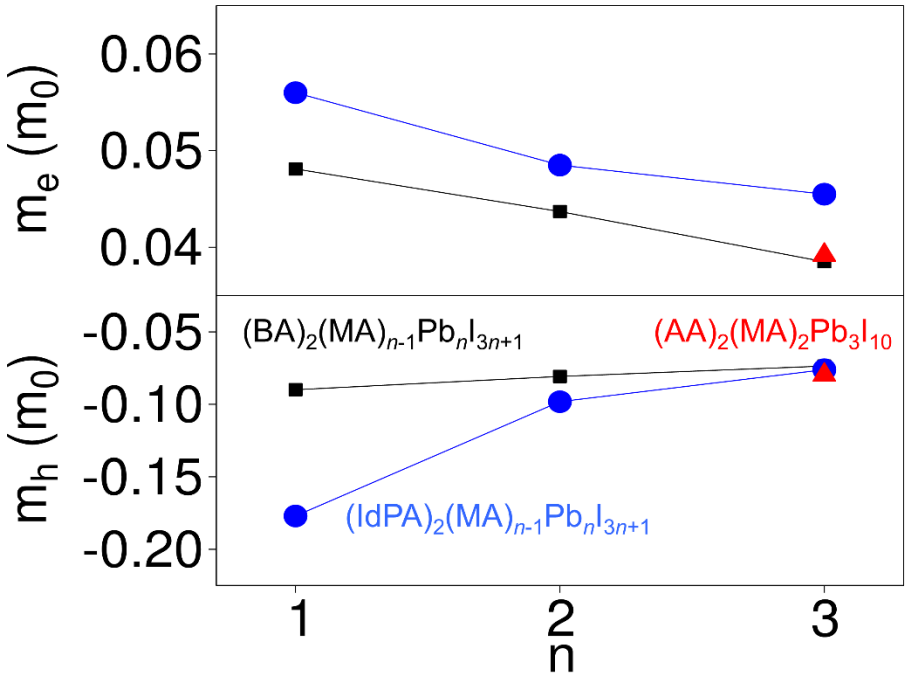

Figure S14. Computed electron (m_e) and hole (m_h) effective masses for the $(IdPA)_2(MA)_{n-1}Pb_nI_{n+1}$ (n=1-3) series (blue circles), $(AA)_2(MA)_2Pb_3I_{10}$ (red triangle) and the $(BA)_2(MA)_{n-1}Pb_nI_{n+1}$ (n=1-3) series (black squares).

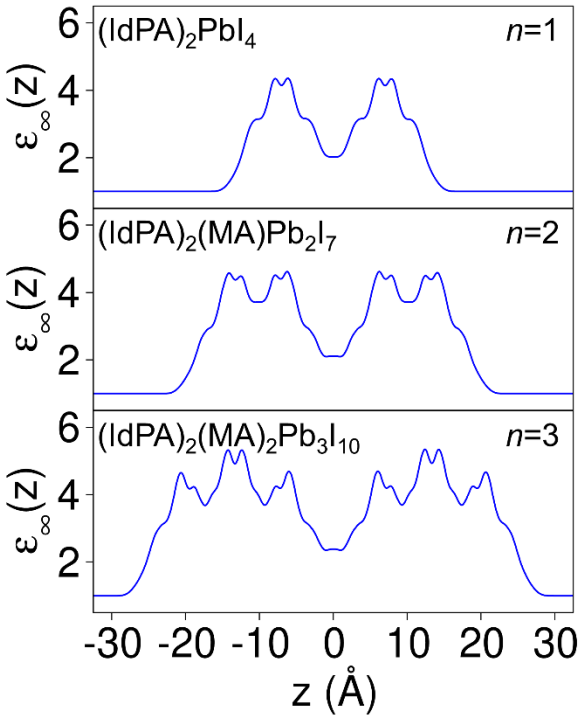

Figure S15. Computed high-frequency dielectric constant profile along the stacking axis for the IdPA)$_2$(MA)$_{n-1}$Pb$_n$I $_{n+1}$ (n=1-3) series.

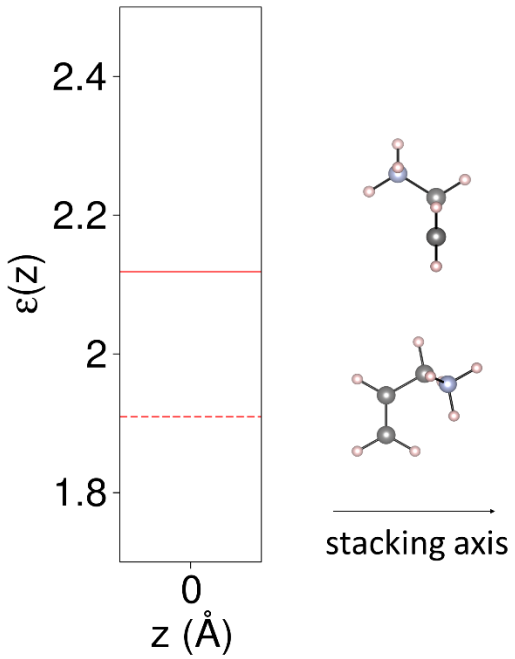

Figure S16. Computed high-frequency dielectric constant profile along the stacking axis for the AA cation with different orientations. When the plan containing the unsaturated bond is perpendicular to the stacking axis, the dielectric response goes from 1.90 to 2.10.

3.5 Optical Data

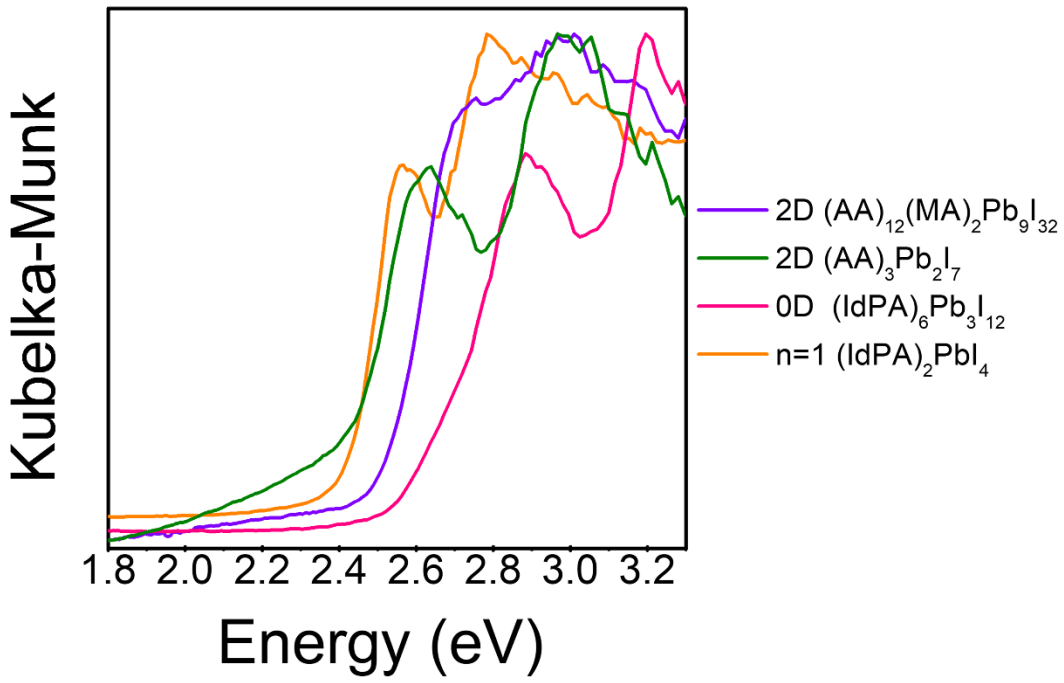

Figure S17. Optical absorption spectra of $(IdPA)_2PbI_4$ (n=1) along with perovskitoids $(AA)_3Pb_2I_7$, $(AA)_{12}(MA)_2Pb_9I_{32}$ and $(IdPA)_6Pb_3I_{32}$.

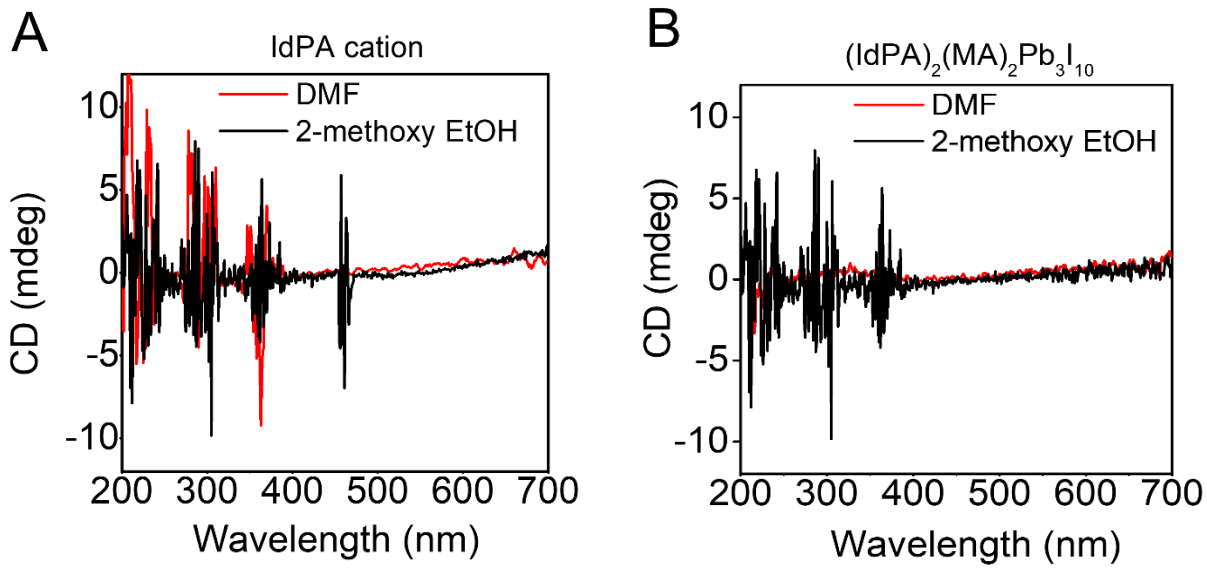

Figure S18. (A) Circular dichroism (CD) spectra of IdPA cation measured in DMF and 2-methoxyethanol, respectively. (**B**) CD spectra of $(IdPA)_2(MA)_2Pb_3I_{10}$ perovskite measured in DMF and 2-methoxyethanol, respectively. CD measures differential absorption of left and right

circularly polarized light passing through a chiral molecule to indicate the absolute configuration of chiral enantiomers that present non-zero CD signal.[13] In both **(A)** and **(B)** spectra here, the CD signals are negligible, pointing to a racemic mixture.

3.6 NMR Spectroscopy

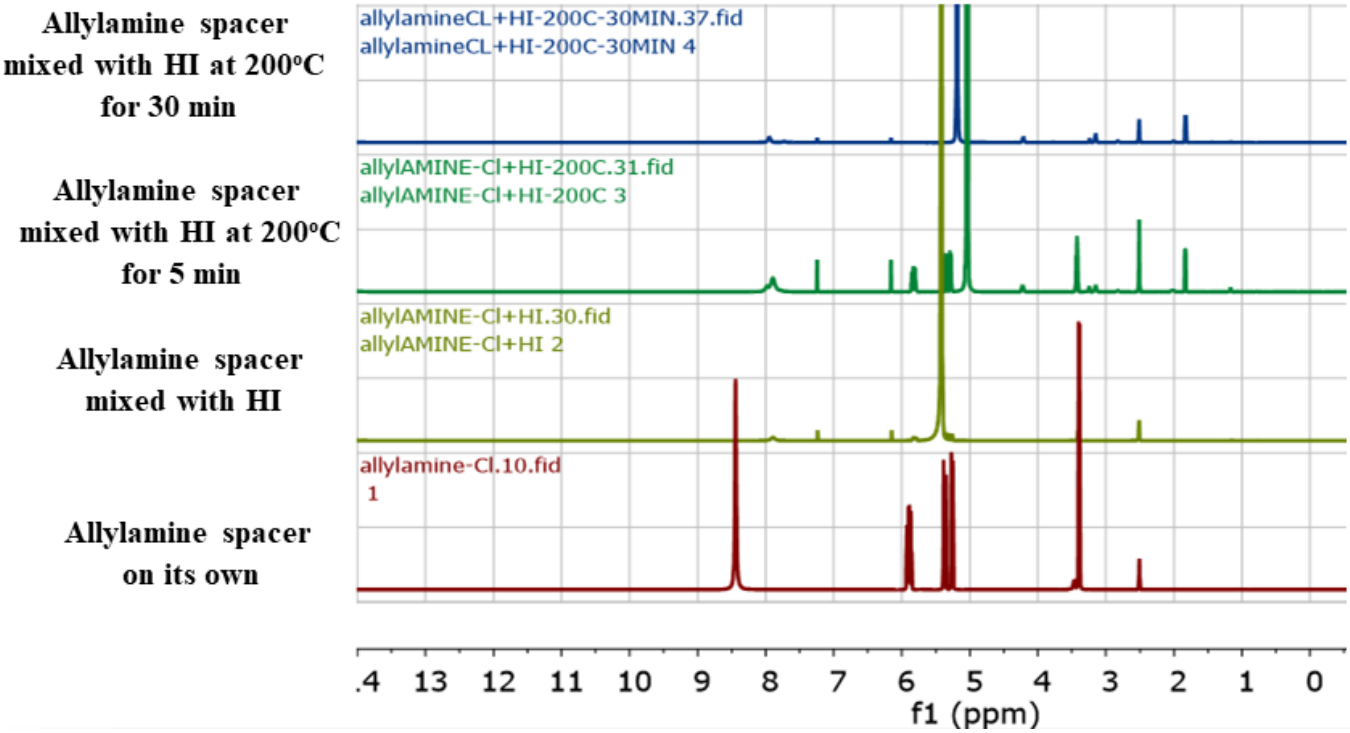

Figure S19. Proton NMR spectra of AA in HI/H_3PO_2 solution, as control experiment, mimicking the conditions in the different steps of the perovskite synthesis.

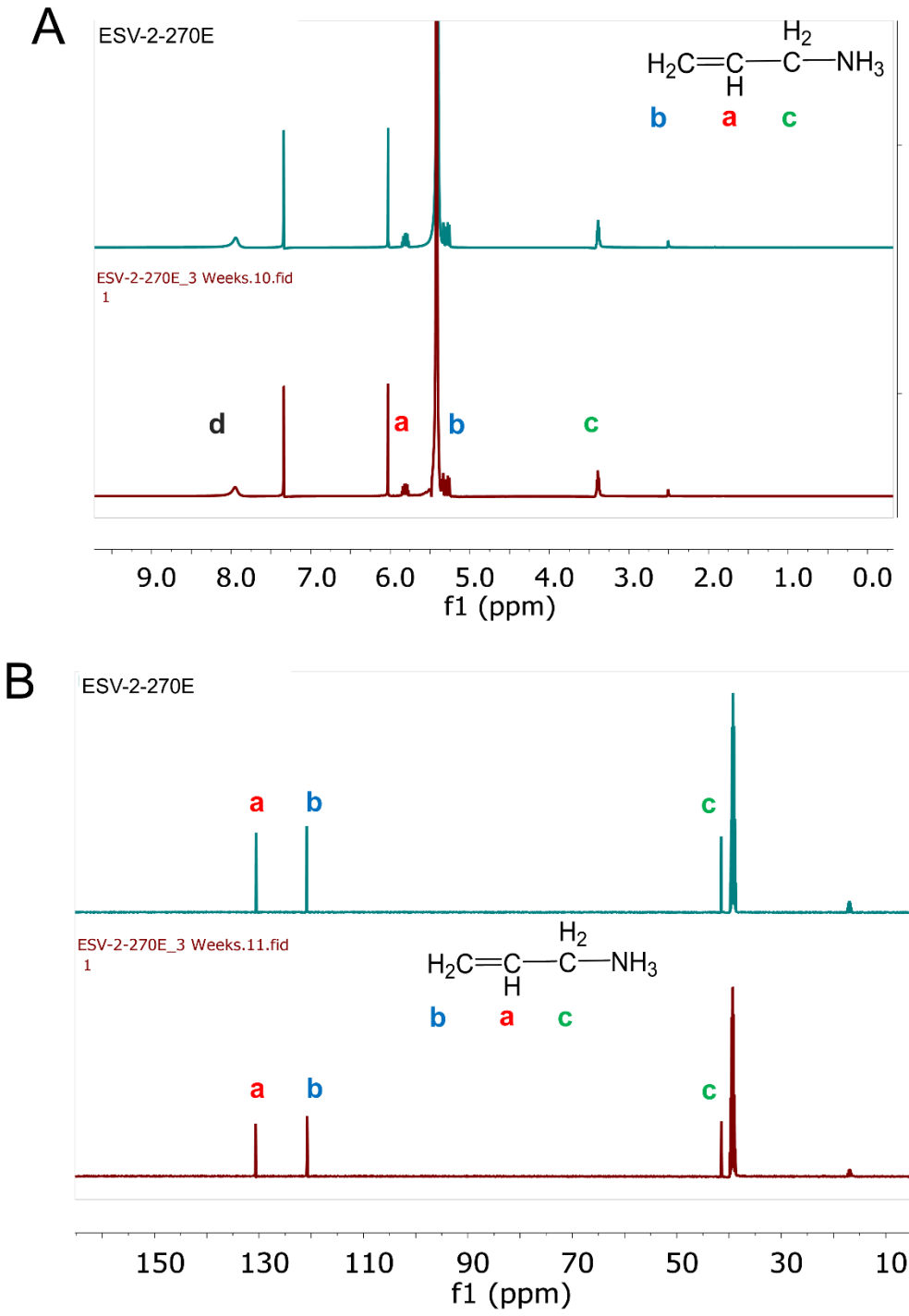

Figure S20. (A) Comparison of proton NMR spectra of $AA^{+}Cl^{-}$ in HI/H_3PO_2 solution immediately after dissolution at R.T. and after 3 weeks in HI/H_3PO_2 solution, respectively. Peak at δ≈2.5 ppm corresponds to NMR solvent d-DMSO while singlet peaks at δ≈6.1 ppm and δ≈7.4 ppm corresponds to H_3PO_2 **(B)** Comparison of carbon NMR spectra of $AA^{+}Cl^{-}$ in HI/H_3PO_2 solution immediately after dissolution at R.T. and after 3 weeks in HI/H_3PO_2 solution, respectively. Peak

at δ≈25 ppm corresponds to NMR solvent d-DMSO.

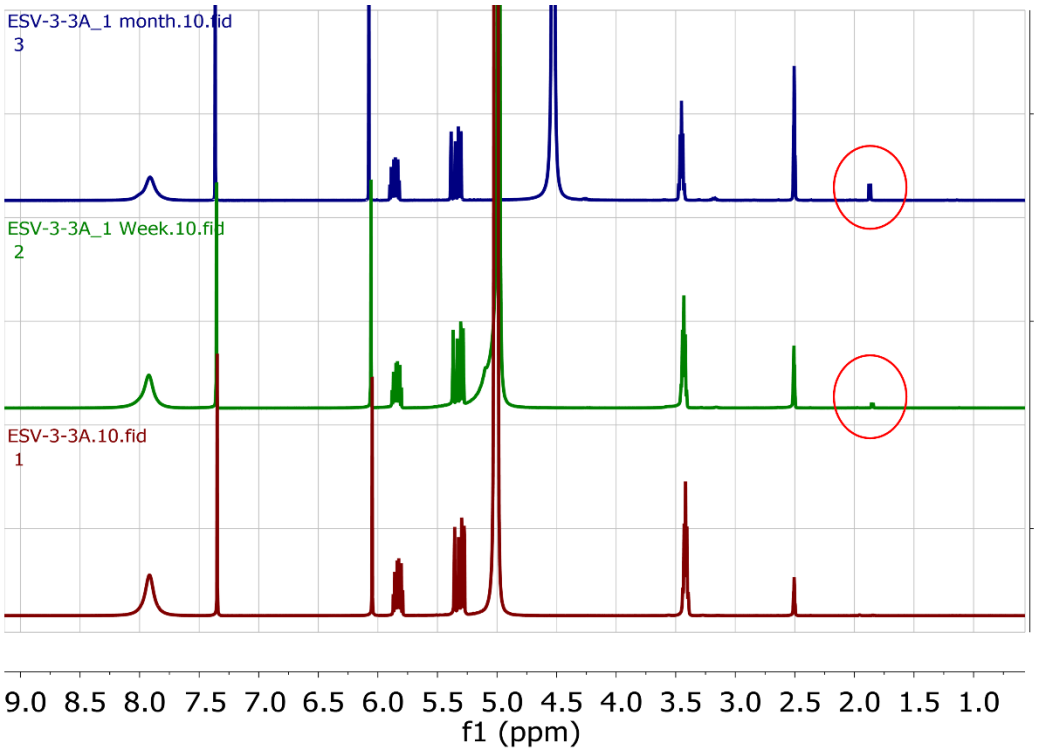

Figure S21. From bottom-up, comparison of proton NMR spectra of reaction solution ESV-3-3A immediately after dissolution at 200°C (as indicated on hotplate) for 5 minutes, after 1 week and after 1 month respectively. Reaction solution ESV-3-3A consists of $AA^{+}Cl^{-}$ in HI/H_3PO_2 solution heated at 200°C for 5 min. After 1 week, reaction solution ESV-3-3A has a peak at δ≈1.8 ppm (circled in red) corresponding to the IdPA cation.

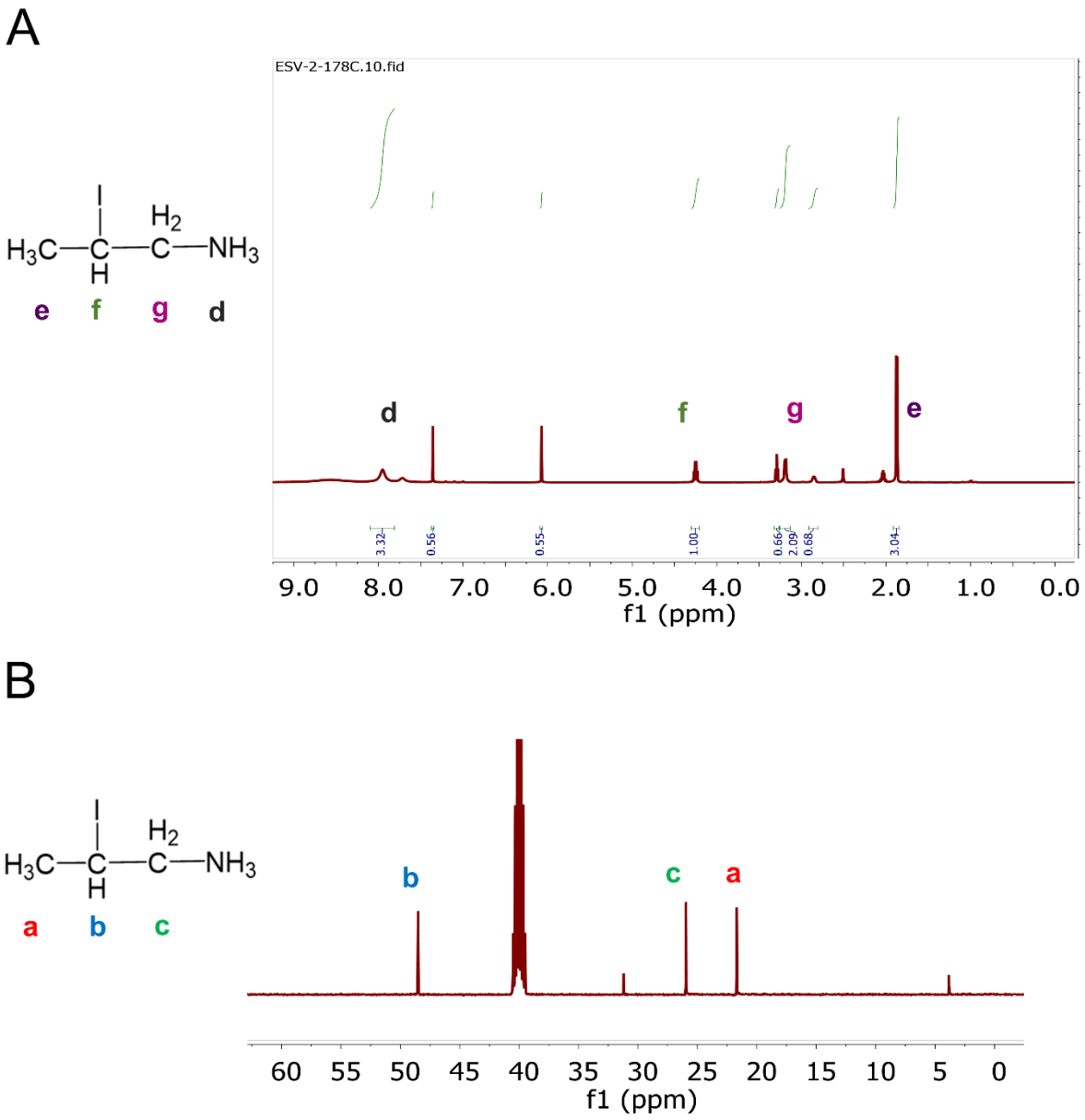

Figure S22. (A) ^{1}H NMR spectra of IdPA cation (2-iodopropylammonium). Peak at δ≈2.5 ppm corresponds to NMR solvent d-DMSO while singlet peaks at δ≈6.1 ppm and δ≈7.4 ppm corresponds to H_3PO_2 **(B) (B)** ^{13}C NMR spectra of IdPA cation. Peak at δ≈25 ppm corresponds to NMR solvent d-DMSO. Remaining peaks at δ≈30 ppm and δ≈5 ppm correspond to the minority product 1-iodopropylammonium.

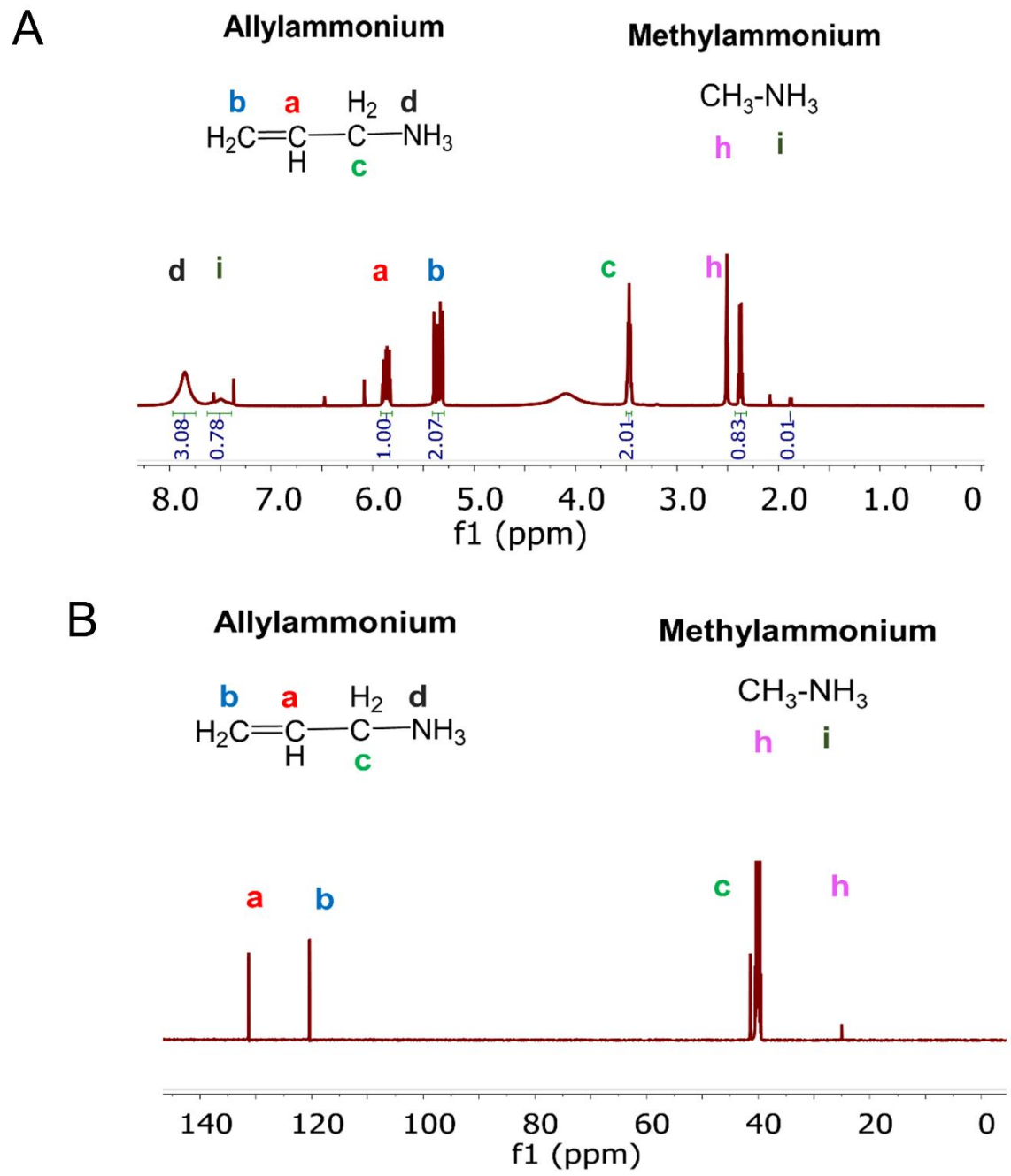

Figure S23. (A) ^{1}H NMR spectra of $(AA)_2(MA)_2Pb_3I_{10}$ (n=3). **(B)** ^{13}C NMR spectra of $(AA)_2(MA)_2Pb_3I_{10}$ (n=3).

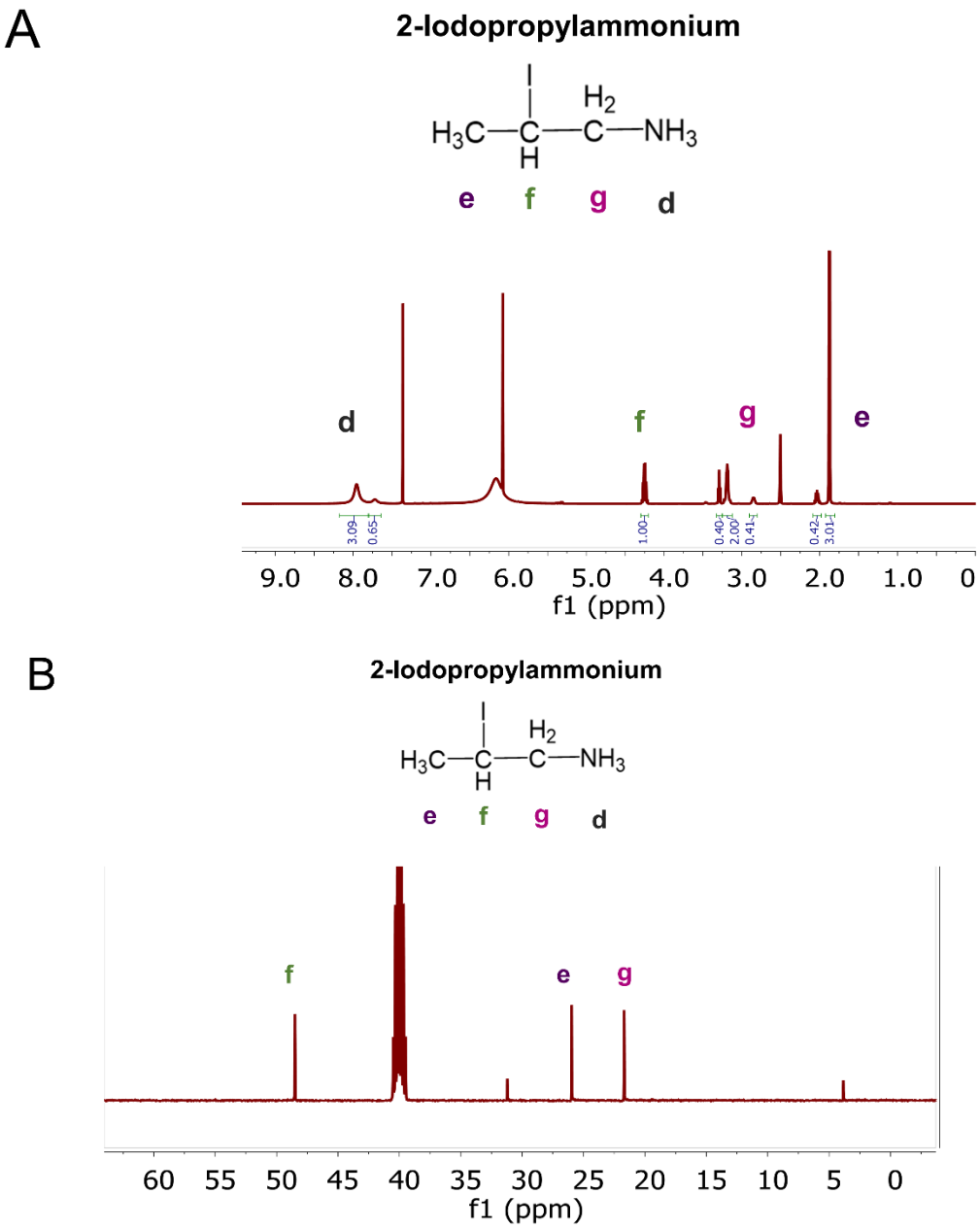

Figure S24. ^{1}H NMR spectra of $(IdPA)_2PbI4$ (*n* =1). **(B)** ^{13}C NMR spectra of $(IdPA)_2PbI4$ (*n* =1).

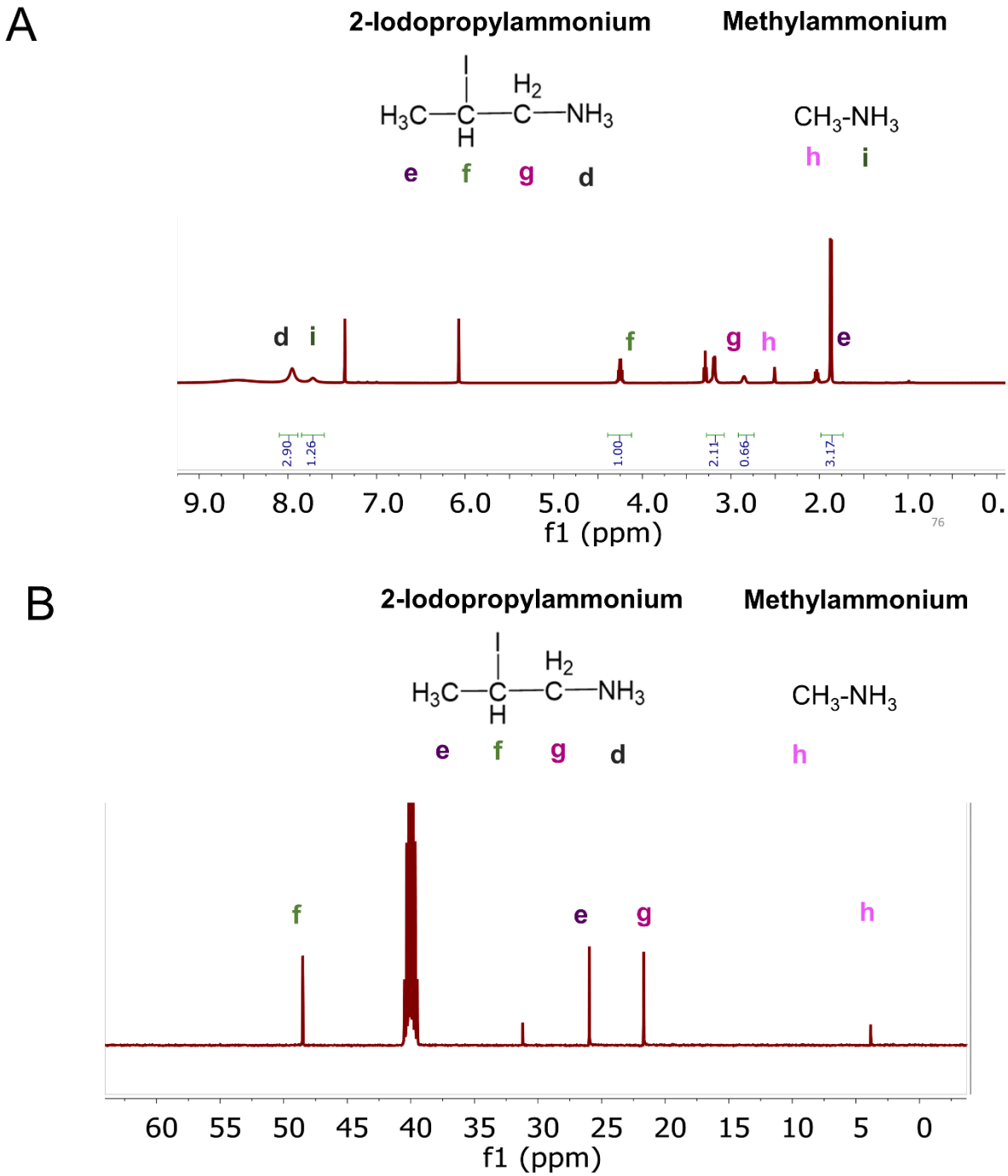

Figure S25. ^{1}H NMR spectra of $(IdPA)_2(MA)Pb_2I_7$ (n =2). **(B)** ^{13}C NMR spectra of $(IdPA)_2(MA)Pb_2I_7$ (n =2).

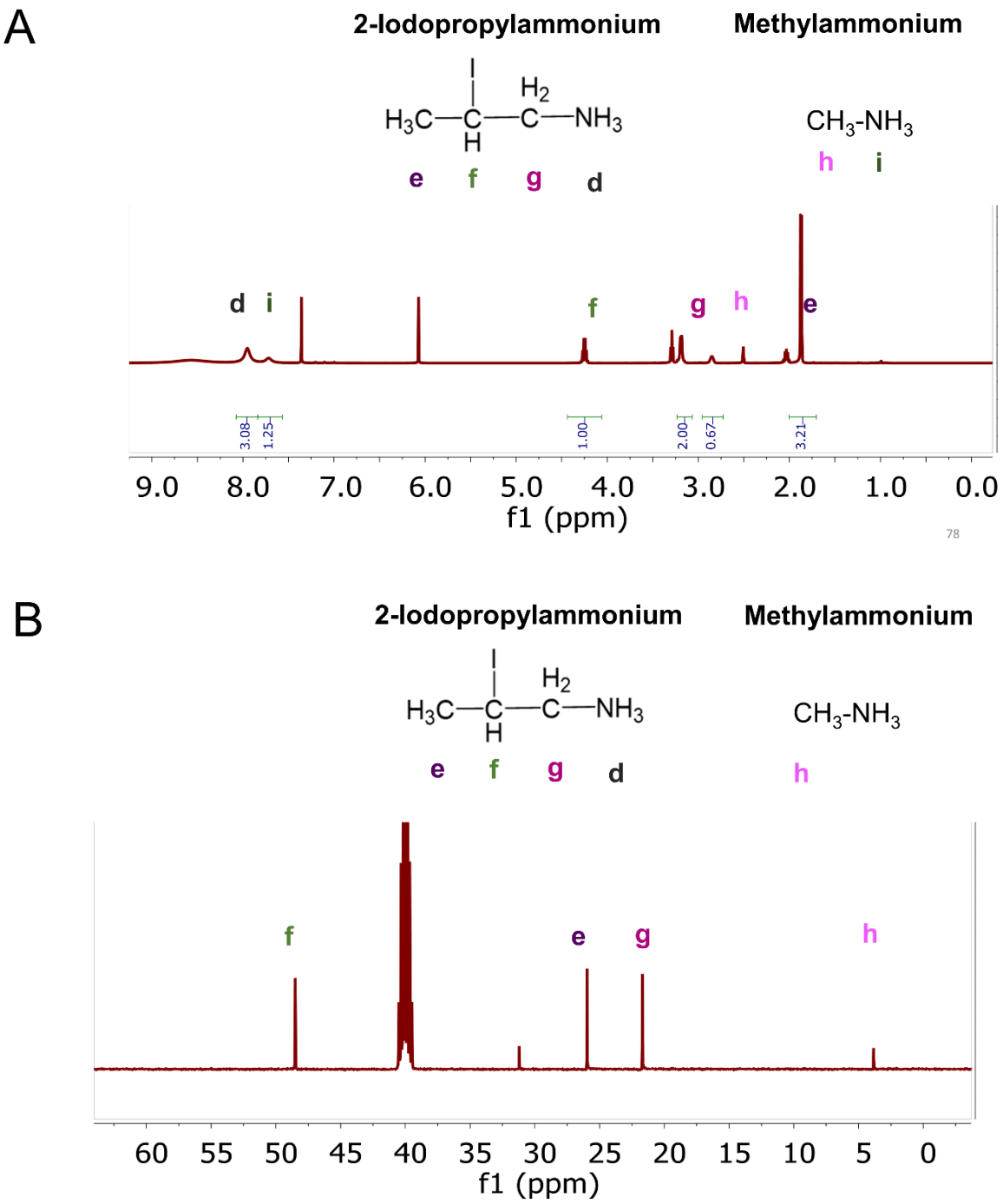

Figure S26. ^{1}H NMR spectra of $(IdPA)_2(MA)_2Pb_3I_{10}$ (n=3). **(B)** ^{13}C NMR spectra of $(IdPA)_2(MA)_2Pb_3I_{10}$ (n=3).

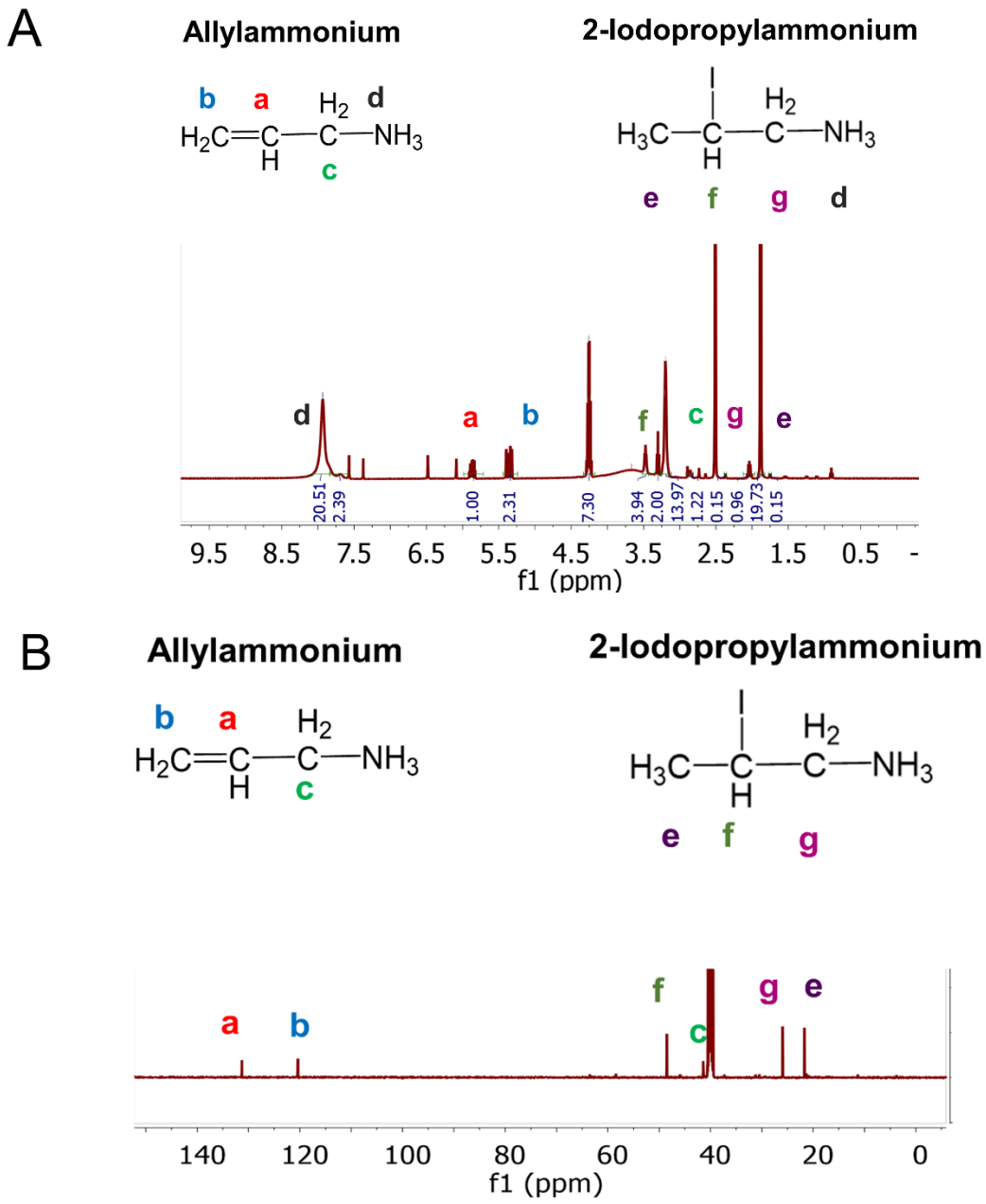

Figure S27. ^{1}H NMR spectra of $[(AA)_x(IdPA)_{1-x}]_2PbI_4$ (n=1). **(B)** ^{13}C NMR spectra of $[(AA)_x(IdPA)_{1-x}]_2PbI_4$ (n=1).

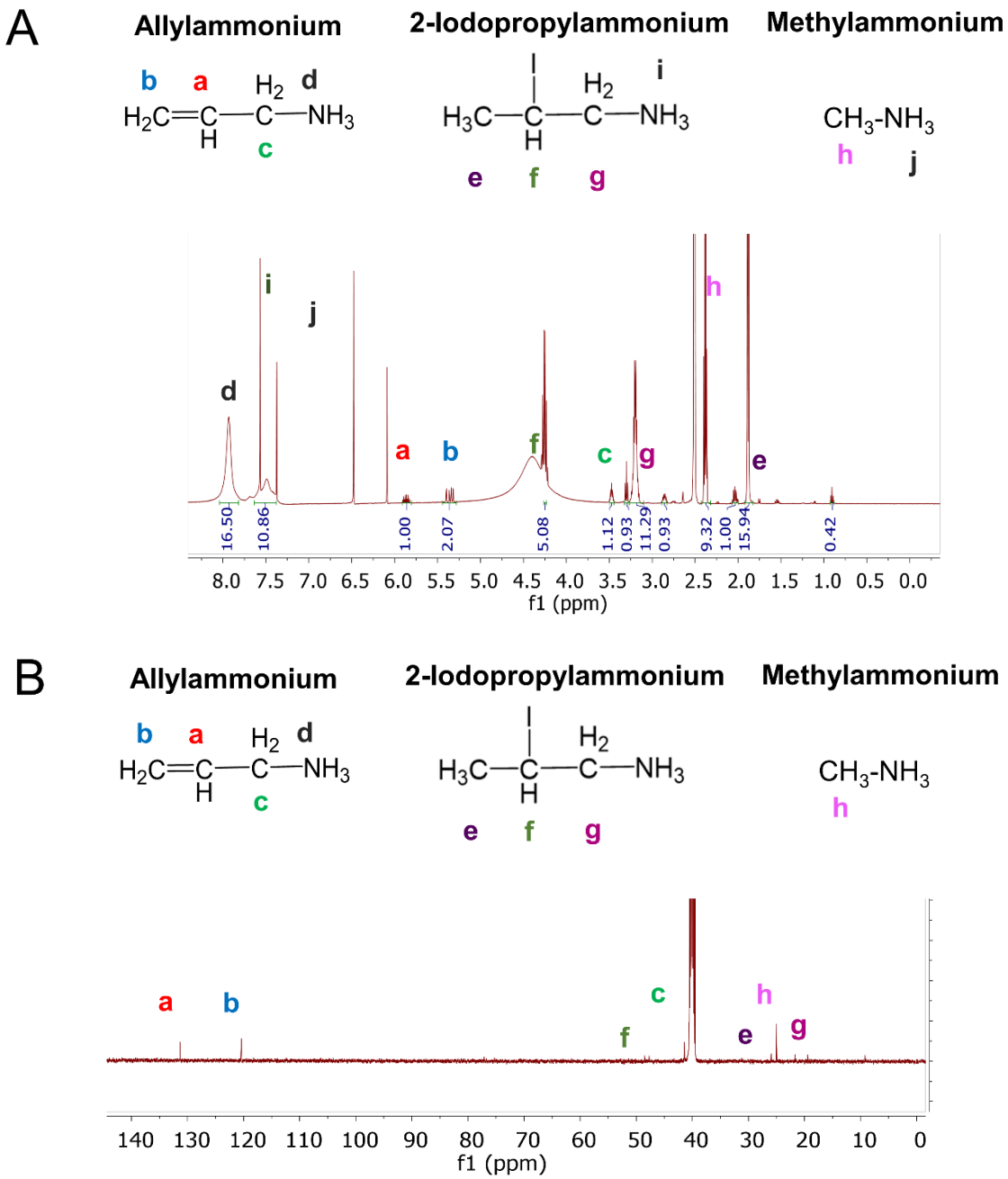

Figure S28. ^{1}H NMR spectra of $[(AA)_x(IdPA)_{1-x}]_2(MA)Pb_2I_7$ (n=2). **(B)** ^{13}C NMR spectra $[(AA)_x(IdPA)_{1-x}]_2(MA)Pb_2I_7$ (n=2).

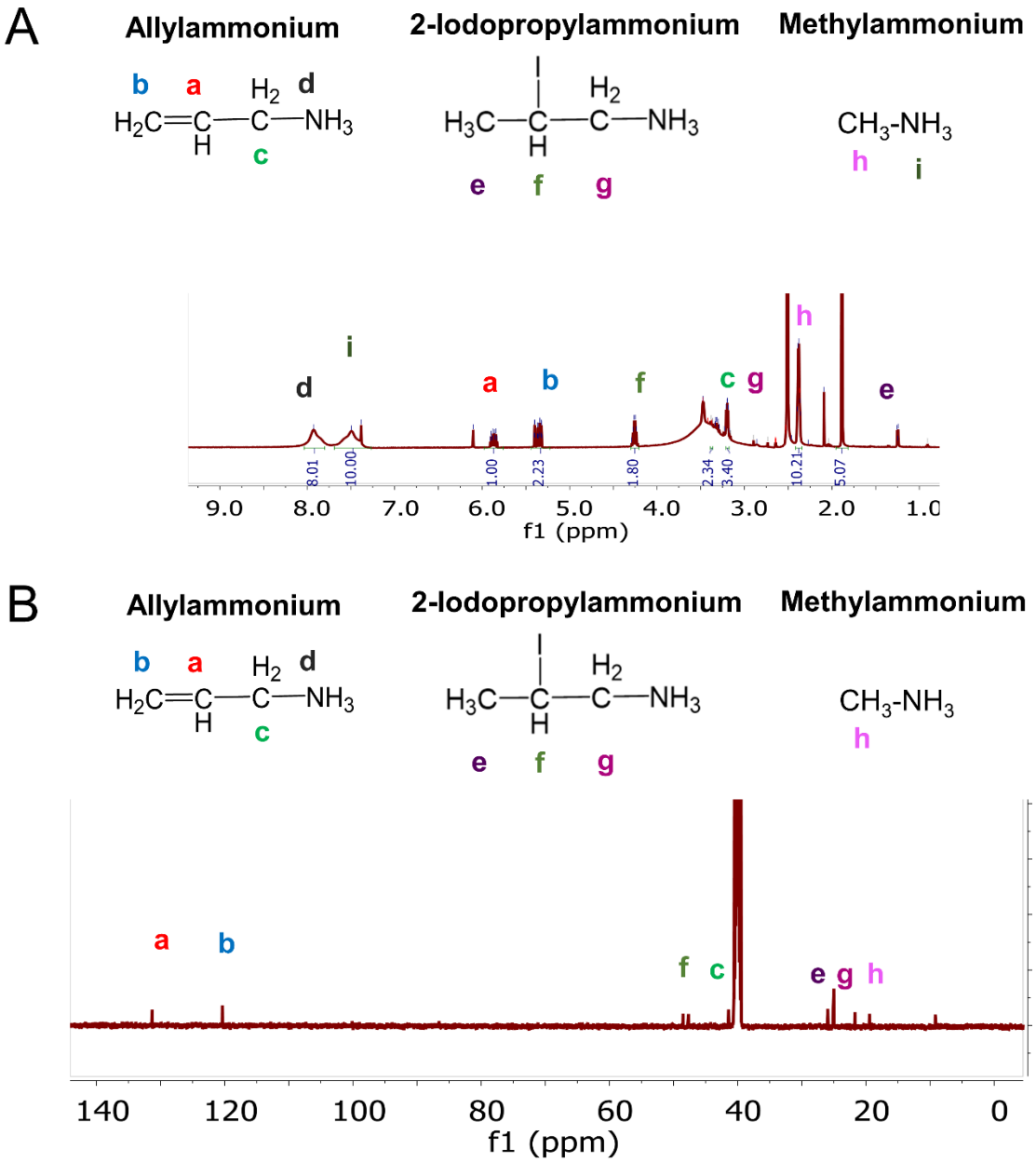

Figure S29. (A) ^{1}H NMR spectra of $[(AA)_x(IdPA)_{1-x}]_2$ $(MA)_2Pb_3I_{10}$ (n=3). **(B)** ^{13}C NMR spectra $[(AA)_x(IdPA)_{1-x}]_2$ $(MA)_2Pb_3I_{10}$ (n=3).

3.7 SEM and Microscope Images

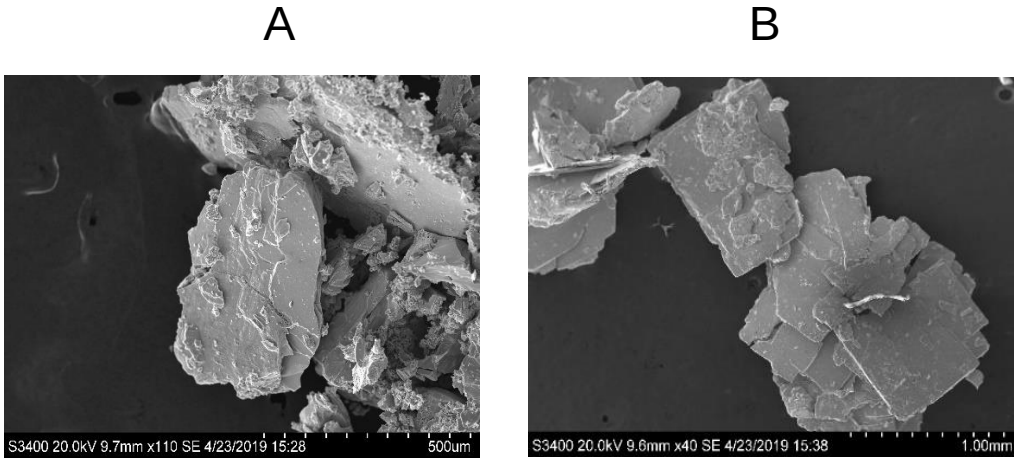

Figure S30. SEM images of crystals of **(A)** $(AA)_2MA_2Pb_3I_{10}$ (*n*=3), **(B)** $(AA)_2MA_3Pb_4I_{13}$ (*n*=4).

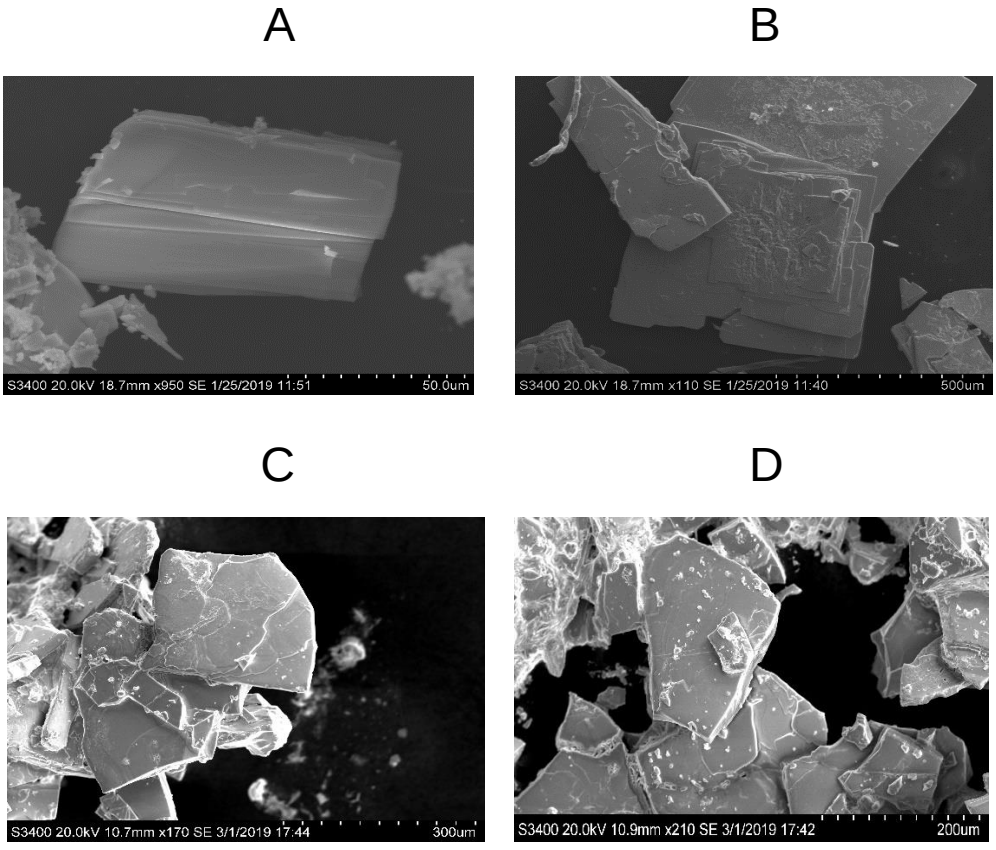

Figure S31. SEM images of crystals of **(A)** $[(AA)_x(IdPA)_{1-x}]_2PbI_4$ (*n*=1), **(B)** $[(AA)_x(IdPA)_{1-x}]_2MAPb_2I_7$ (*n*=2), **(C)** $[(AA)_x(IdPA)_{1-x}]_2MA_2Pb_3I_{10}$ (*n*=3), **(D)** $[(AA)_x(IdPA)_{1-x}]_2MA_3Pb_4I_{13}$ (*n*=4).

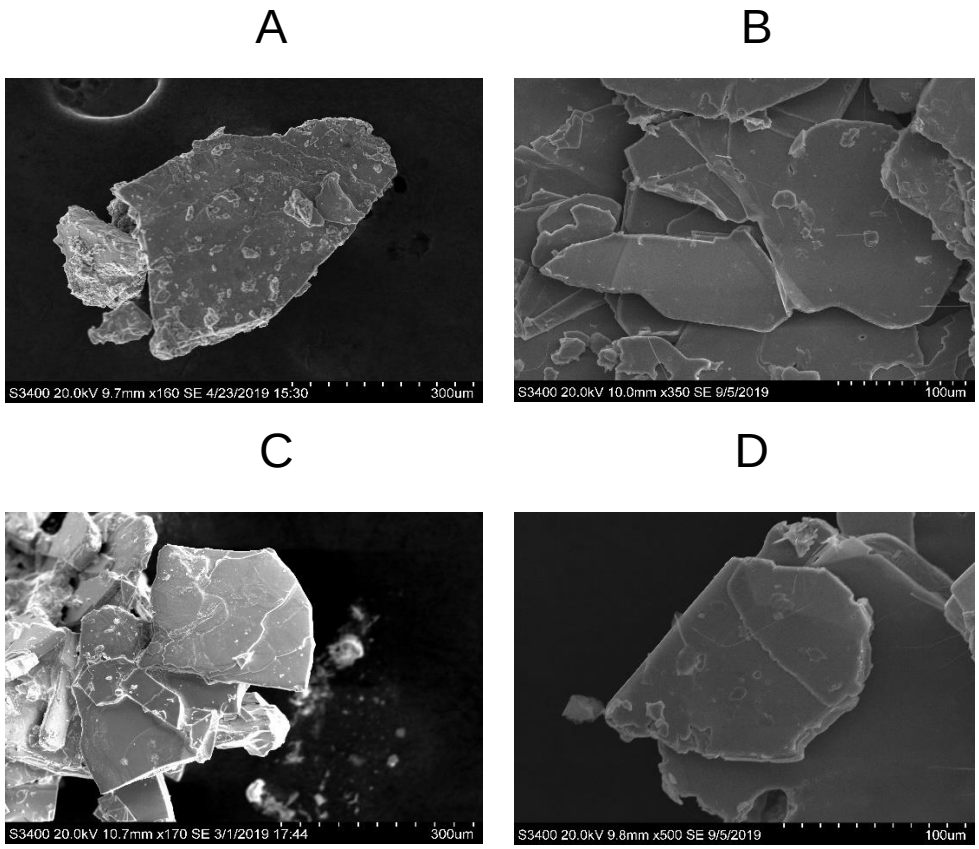

Figure S32. SEM images of crystals of (**A**) $(IdPA)_2PbI_4$ (*n*=1), (**B**) $(IdPA)_2MAPb_2I_7$ (*n*=2), (**C**) $(IdPA)_2MA_2Pb_3I_{10}$ (*n*=3), (**D**) $(IdPA)_2MA_3Pb_4I_{13}$ (*n*=4).

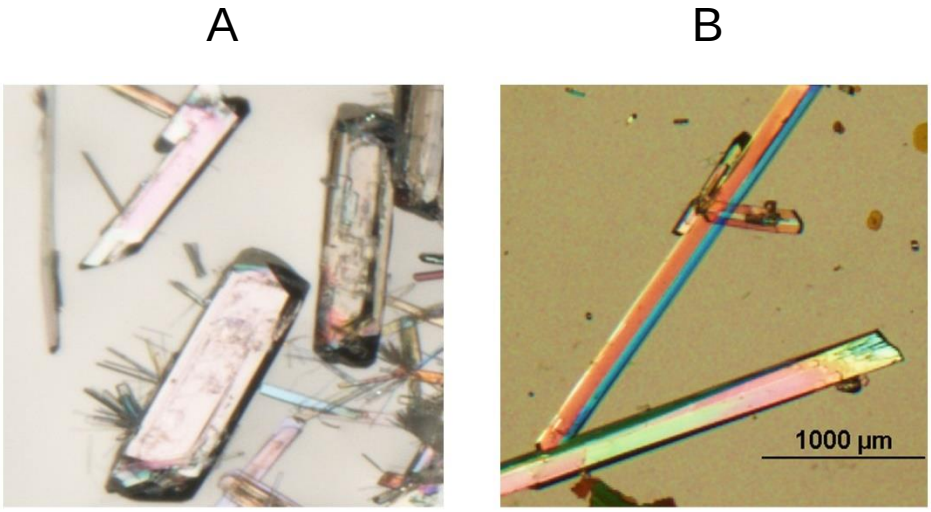

Figure S33. Microscope images of crystals of 2D structures with mixed corner- and face-sharing connectivity **(A)** $(AA)_3Pb_2I_7$ **(B)** $(AA)_{12}(MA)_2Pb_9I_{32}$.

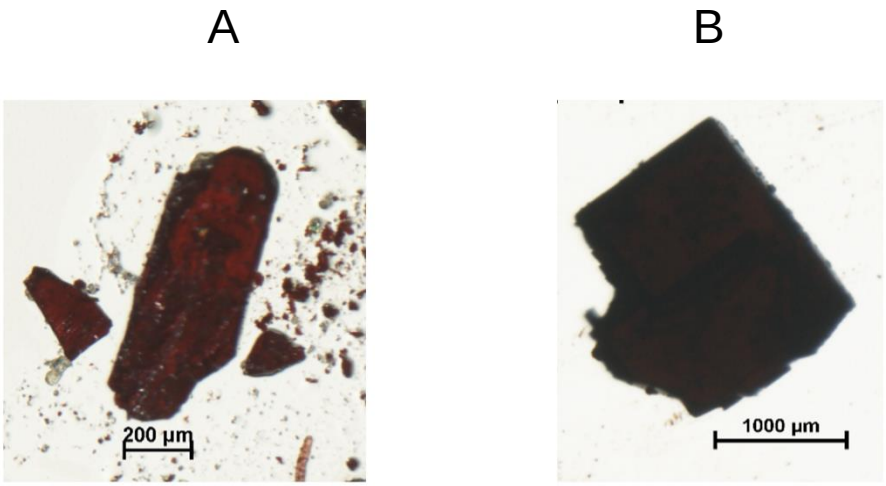

Figure S34. Microscope images of crystals of **(A)** $(AA)_2MA_2Pb_3I_{10}$ (*n*=3), **(B)** $(AA)_2MA_3Pb_4I_{13}$ (*n*=4).

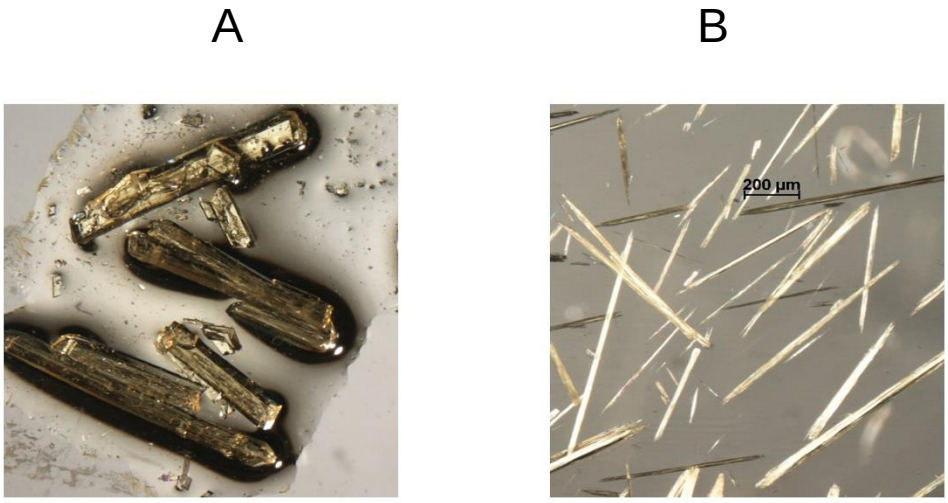

Figure S35. Microscope images of crystals of **(A)** $(IdPA)_6Pb_3I_{12}$ and **(B)** $(IdPA)PbI_3$.

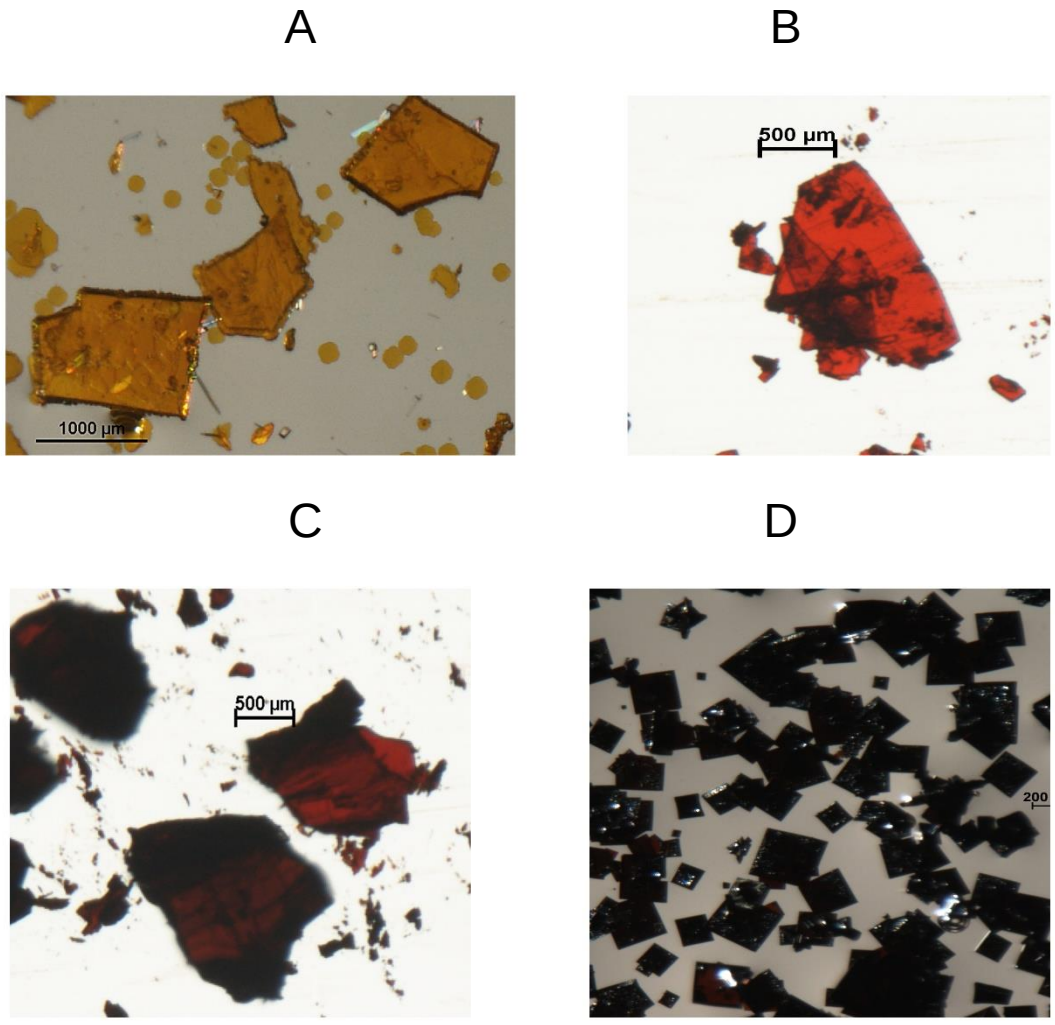

Figure S36. Microscope images of crystals of **(A)** $(IdPA)_2PbI_4$, **(B)** $(IdPA)_2(MA)Pb_2I_7$, **(C)** $(IdPA)_2(MA)_2Pb_3I_{10}$ and **(D)** $(IdPA)_2(MA)_3Pb_4I_{13}$.

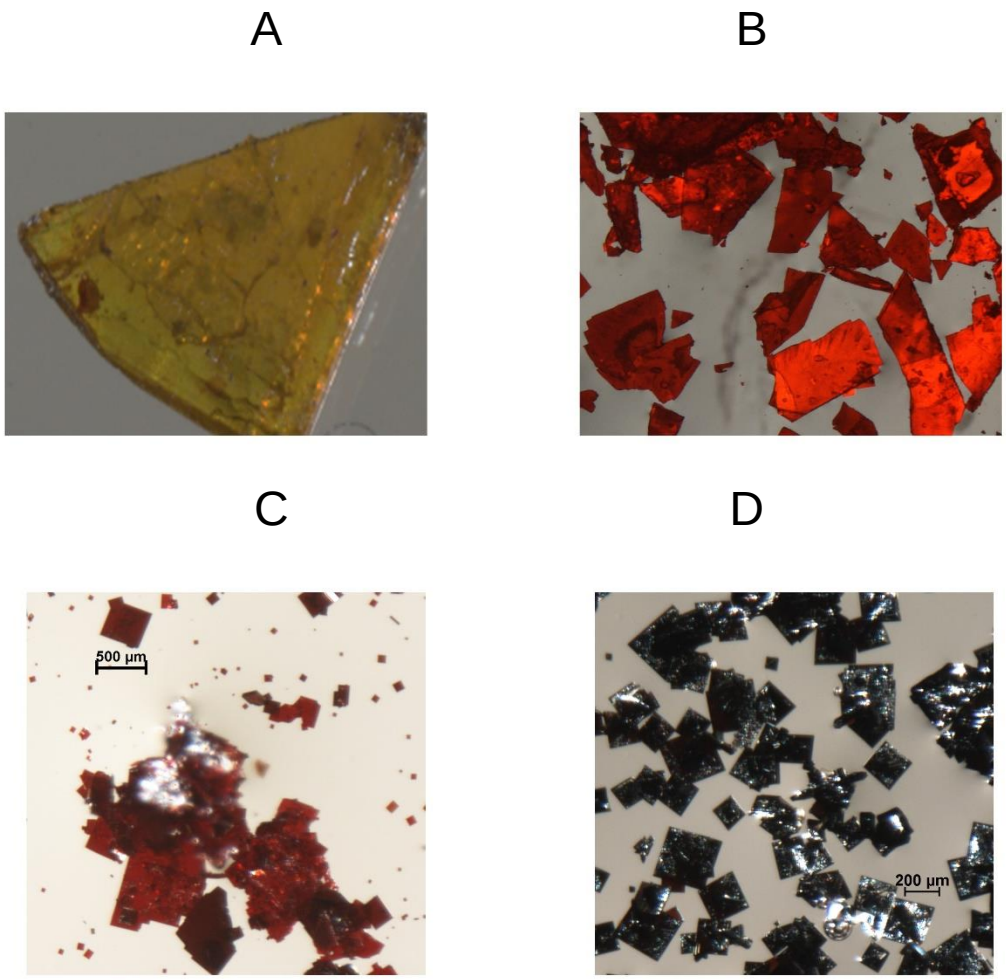

Figure S37. Microscope images of crystals of **(A)** $[(AA)_x(IdPA)_{1-x}]_2PbI_4$, **(B)** $[(AA)_x(IdPA)_{1-x}]_2(MA)Pb_2I_7$, **(C)** $[(AA)_x(IdPA)_{1-x}]_2(MA)_2Pb_3I_{10}$ and **(D)** $[(AA)_x(IdPA)_{1-x}]_2(MA)_3Pb_4I_{13}$.

3.8 Crystallographic Tables

Table S4. Pb-I bond distances (Å) and Pb-I-Pb angles (º) for $(AA)_3Pb_2I_7$.

Label	Distances	Label	Angles (º)
Pb(1)-I(1)	3.2455(14)	Pb(1)-I(1)-Pb(2)	77.44(3)
Pb(1)-I(2)	3.1733(15)	Pb(1)-I(3)-Pb(2)	78.25(3)
Pb(1)-I(3)	3.2283(13)	Pb(1)-I(4)-Pb(2)	78.22(3)
Pb(1)-I(4)	3.2424(13)	Pb(2)#3-I(6)-Pb(1)	167.53(8)
Pb(1)-I(6)	3.2263(16)	Pb(2)#4-I(7)-Pb(1)	155.39(7)
Pb(1)-I(7)	3.1767(15)		
Pb(2)-I(1)	3.3149(15)		
Pb(2)-I(3)	3.2758(14)		
Pb(2)-I(4)	3.2635(14)		
Pb(2)-I(5)	3.0981(18)		
Pb(2)-I(6)#1	3.1847(17)		
Pb(2)-I(7)#2	3.1393(15)		

Table S5. Pb-I bond distances (Å) and Pb-I-Pb angles (º) for $(AA)_{12}(MA)_2Pb_9I_{32}$.

Label	Distances	Label	Angles (º)
Pb(01)-I(00A)	3.2074(16)	Pb(03)-I(006)-Pb(04)	77.13(4)
Pb(01)-I(00D)	3.1737(15)	Pb(03)-I(007)-Pb(04)	77.38(4)
Pb(01)-I(00E)	3.1722(16)	Pb(04)-I(008)-Pb(03)#3	74.96(4)
Pb(01)-I00H()#1	3.2659(15)	Pb(01)-I(00A)-Pb(03)#4	174.45(5)
Pb(01)-I(00I)	3.0844(15)	Pb(02)-I(00C)-Pb(05)	169.48(5)
Pb(01)-I(00K)	3.1487(15)	Pb(01)-I(00D)-Pb(03)	158.91(5)
Pb(02)-I(00C)	3.1679(17)	Pb(01)-I(00E)-Pb(02)	170.05(5)
Pb(02)-I(00E)	3.2186(16)	Pb(02)-I(00F)-Pb(05)#4	154.38(5)
Pb(02)-I(00F)	3.1212(15)	Pb(02)-I00H()-Pb(01)#1	166.61(5)
Pb(02)-I00H()	3.2530(15)	Pb(01)-I(00K)-Pb(02)#4	162.91(6)
Pb(03)-I(006)	3.1673(17)		
Pb(03)-I(007)	3.1743(15)		
Pb(03)-I(008)#3	3.3163(14)		
Pb(03)-I(00A)#2	3.2483(17)		
Pb(03)-I(00B)	3.1526(14)		
Pb(03)-I(00D)	3.1964(15)		

Pb(04)-I(006)#3	3.2374(14)
Pb(04)-I(006)	3.2374(14)
Pb(04)-I(007)	3.2138(17)
Pb(04)-I(007)#3	3.2139(16)
Pb(04)-I(008)	3.2455(13)
Pb(04)-I(008)#3	3.2456(13)
Pb(05)-I(009)	3.0818(15)
Pb(05)-I(00C)	3.3828(16)
Pb(05)-I(00F)#2	3.4273(15)
Pb(05)-I(00G)	3.0744(15)
Pb(05)-I(00J)	2.9917(15)

Table S6. Pb-I bond distances (Å) and Pb-I-Pb angles (º) for $(AA)_2(MA)_2Pb_3I_{10}$ (n=3).

Label	**Distances**	**Label**	**Angles (º)**
Pb(1)-I(2)	3.1608(17)	Pb(2)-I(1)-Pb(2)#7	169.96(8)
Pb(1)-I(2)#1	3.1608(17)	Pb(1)-I(2)-Pb(2)	166.74(8)
Pb(1)-I(5)	3.174(2)	Pb(2)-I(3)-Pb(2)#3	162.34(9)
Pb(1)-I(5)#2	3.175(2)	Pb(1)-I(5)-Pb(1)#9	165.32(8)
Pb(1)-I(5)#1	3.174(2)		
Pb(1)-I(5)#3	3.175(2)		
Pb(2)-I(1)	3.1801(19)		
Pb(2)-I(1)#4	3.1777(19)		
Pb(2)-I(2)	3.3027(19)		
Pb(2)-I(3)	3.171(2)		
Pb(2)-I(3)#5	3.165(2)		
Pb(2)-I(4)	3.053(2)		
Pb(1)-I(2)	3.1608(17)		
Pb(1)-I(2)#1	3.1608(17)		
Pb(1)-I(5)	3.174(2)		
Pb(1)-I(5)#2	3.175(2)		
Pb(1)-I(5)#1	3.174(2)		
Pb(1)-I(5)#3	3.175(2)		
Pb(2)-I(1)	3.1801(19)		
Pb(2)-I(1)#4	3.1777(19)		
Pb(2)-I(2)	3.3027(19)		

Pb(2)-I(3)	3.171(2)
Pb(2)-I(3)#5	3.165(2)
Pb(2)-I(4)	3.053(2)

Table S7. Pb-I bond distances (Å) and Pb-I-Pb angles (º) for $(IdPA)_2PbI_4$ (*n* =1).

Label	Distances	Label	Angles (º)
Pb1-I2#1	3.1970(11)	Pb(1)#4-I(2)-Pb(1)	152.71(5)
Pb1-I3	3.160(5)		
Pb1-I3	3.160(5)		
Pb1-I2	3.1970(11)		
Pb1-I2#2	3.2062(15)		
Pb1-I2#3	3.1970(11)		

Table S8. Pb-I bond distances (Å) and Pb-I-Pb angles (º) for $(IdPA)_2(MA)Pb_2I_7$ (*n* =2).

Label	Distances	Label	Angles (º)
Pb1—I1	3.2679(7)	Pb(1)#4-I(2)-Pb(1)	178.92(8)
Pb1—I4	3.0993(18)	Pb(1)#5-I(6)-Pb(1)	156.45(5)
Pb1—I2	3.2006(12)	Pb(1)-I(7)-Pb(1)#6	156.29(6)
Pb1—I2#1	3.2031(12)		
Pb1—I3#2	3.1843(13)		
Pb1—I3	3.1859(12)		

Table S9. Pb-I bond distances (Å) and Pb-I-Pb angles (º) for $(IdPA)_2(MA)_2Pb_3I_{10}$ (*n*=3) .

Label	Distances	Label	Angles (º)
Pb(01)-I(004)	3.1803(18)	Pb(02)-I(003)-Pb(02)#6	157.66(8)
Pb(01)-I(004)#1	3.1899(18)	Pb(01)-I(004)-Pb(01)#7	158.37(9)
Pb(01)-I(004)#2	3.1804(18)	Pb(01)-I(005)-Pb(02)	179.18(10)
Pb(01)-I(004)#3	3.1899(18)	Pb(02)#5-I(006)-Pb(02)	158.02(9)
Pb(01)-I(005)#2	3.180(2)		
Pb(01)-I(005)	3.180(2)		
Pb(02)-I(003)#4	3.1938(19)		
Pb(02)-I(003)	3.1928(19)		
Pb(02)-I(005)	3.288(2)		

Pb(02)-I(006)#1	3.181(2)
Pb(02)-I(006)	3.184(2)
Pb(02)-I(007)	3.082(3)

Table S10. Pb-I bond distances (Å) and Pb-I-Pb angles (º) for (IdPA)PbI_3.

Label	Distances	Label	Angles (º)
Pb(1)-I(2)#1	3.251(2)	Pb(1)-I(2)-Pb(1)#2	93.52(5)
Pb(1)-I(2)	3.213(2)	Pb(1)-I(5)-Pb(1)#2	92.22(5)
Pb(1)-I(3)	3.043(2)		
Pb(1)-I(5)	3.2351(19)		
Pb(1)-I(5)#1	3.299(2)		

Table S11. Pb-I bond distances (Å) and Pb-I-Pb angles (º) for $(IPA)_6Pb_3I_{12}$.

Label	Distances	Label	Angles (º)
Pb(1)-I(7)	3.2690(11)	Pb(1)-I(8)-Pb(3)	76.71(3)
Pb(1)-I(8)	3.1985(12)	Pb(1)-I(12)-Pb(3)	76.34(3)
Pb(1)-I(12)	3.1630(12)	Pb(1)-I(20)-Pb(2)	75.69(3)
Pb(1)-I(14)	3.3448(13)	Pb(1)-I(1)-Pb(2)	78.24(3)
Pb(1)-I(20)	3.2754(12)		
Pb(1)-I(1)	3.1309(12)		
Pb(2)-I(20)	3.4155(13)		
Pb(2)-I(1)	3.3705(12)		
Pb(2)-I(2)	3.0987(13)		
Pb(2)-I(3)	3.0707(14)		
Pb(2)-I(0AA)	3.0447(14)		
Pb(3)-I(8)	3.3560(13)		
Pb(3)-I(12)	3.4140(13)		
Pb(3)-I(19)	3.1170(13)		
Pb(1)-I(7)	3.2690(11)		
Pb(1)-I(8)	3.1985(12)		
Pb(1)-I(12)	3.1630(12)		
Pb(1)-I(14)	3.3448(13)		
Pb(1)-I(20)	3.2754(12)		
Pb(1)-I(1)	3.1309(12)		

Pb(2)-I(20)	3.4155(13)
Pb(2)-I(1)	3.3705(12)
Pb(2)-I(2)	3.0987(13)
Pb(2)-I(3)	3.0707(14)
Pb(2)-I(0AA)	3.0447(14)
Pb(3)-I(8)	3.3560(13)
Pb(3)-I(12)	3.4140(13)
Pb(3)-I(19)	3.1170(13)
Pb(3)-I(4)	3.0737(14)
Pb(3)-I(5)	3.0260(14)

Table S12. Pb-I bond distances (Å) and Pb-I-Pb angles (º) for $[(AA)_x(IdPA)_{1-x}]_2PbI_4$ (*n*=1).

Label	Distances	Label	Angles (º)
Pb(1)-I(1)	3.2059(9)	Pb(1)#4-I(1)-Pb(1)	148.16(4)
Pb(1)-I(1)#1	3.2065(10)		
Pb(1)-I(1)#2	3.2059(9)		
Pb(1)-I(1)#3	3.2065(10)		
Pb(1)-I(2)	3.1828(13)		
Pb(1)-I(2)#2	3.1829(13)		

Table S13. Pb-I bond distances (Å) and Pb-I-Pb angles (º) for $[(AA)_x(IdPA)_{1-x}]_2(MA)Pb_2I_7$ (*n*=2).

Label	Distances	Label	Angles (º)
Pb(1)-I(1)	3.195(7)	Pb(1)-I(1)-Pb(1)#3	155.8(3)
Pb(1)-I(1)#1	3.191(8)	Pb(1)-I(2)-Pb(2)	177.3(4)
Pb(1)-I(2)	3.24(6)	Pb(2)-I(7)-Pb(2)#3	172.1(14)
Pb(1)-I(4)	3.11(6)	Pb(1)-I(5)-Pb(1)#5	171.8(13)
Pb(1)-I(5)	3.16(2)	Pb(2)-I(3)-Pb(2)#5	156.0(3)
Pb(1)-I(5)#2	3.11(2)		
Pb(2)-I(2)	3.30(6)		
Pb(2)-I(3)	3.206(7)		
Pb(2)-I(3)#2	3.183(7)		
Pb(2)-I(6)	3.12(6)		
Pb(2)-I(7)	3.10(2)		

Pb(2)-I(7)#1	3.16(2)

Table S14. Pb-I bond distances (Å) and Pb-I-Pb angles (º) for $[(AA)_x(IdPA)_{1-x}]_2(MA)_2Pb_3I_{10}$ (*n*=3).

Label	**Distances**	**Label**	**Angles (º)**
Pb(1)-I(3)#1	3.1931(14)	Pb(1)#7-I(3)-Pb(1)	158.28(8)
Pb(1)-I(3)	3.1932(14)	Pb(1)-I(4)-Pb(2)	179.98(8)
Pb(1)-I(3)#2	3.1932(14)	Pb(2)#8-I(5)-Pb(2)	159.67(9)
Pb(1)-I(3)#3	3.1931(14)	Pb(2)-I(6)-Pb(2)#1	159.72(9)
Pb(1)-I(4)	3.1851(18)		
Pb(1)-I(4)#2	3.1850(18)		
Pb(2)-I(4)	3.2987(19)		
Pb(2)-I(5)	3.1876(16)		
Pb(2)-I(5)#4	3.1860(16)		
Pb(2)-I(6)#5	3.1865(16)		
Pb(2)-I(6)	3.1833(16)		
Pb(2)-I(1)	3.073(3)		

4. References

1. Petříček, V.; Dušek, M.; Palatinus, L., Crystallographic Computing System JANA2006: General features. In *Zeitschrift für Kristallographie - Crystalline Materials*, 2014; Vol. 229, p 345.
2. Gate, L. F., Comparison of the Photon Diffusion Model and Kubelka-Munk Equation with the Exact Solution of the Radiative Transport Equation. *Appl. Opt.* **1974,** *13* (2), 236-238.
3. Soler, J. M.; Artacho, E.; Gale, J. D.; García, A.; Junquera, J.; Ordejón, P.; Sánchez-Portal, D., The SIESTA method forab initioorder-Nmaterials simulation. *Journal of Physics: Condensed Matter* **2002,** *14* (11), 2745-2779.
4. Artacho, E.; Anglada, E.; Diéguez, O.; Gale, J. D.; García, A.; Junquera, J.; Martin, R. M.; Ordejón, P.; Pruneda, J. M.; Sánchez-Portal, D.; Soler, J. M., The SIESTA method; developments and applicability. *Journal of Physics: Condensed Matter* **2008,** *20* (6), 064208.
5. Dion, M.; Rydberg, H.; Schröder, E.; Langreth, D. C.; Lundqvist, B. I., Van der Waals Density Functional for General Geometries. *Physical Review Letters* **2004,** *92* (24), 246401.
6. Cooper, V. R., Van der Waals density functional: An appropriate exchange functional. *Physical Review B* **2010,** *81* (16), 161104.
7. Cuadrado, R.; Cerdá, J. I., Fully relativistic pseudopotential formalism under an atomic orbital basis: spin–orbit splittings and magnetic anisotropies. *Journal of Physics: Condensed Matter* **2012,** *24* (8), 086005.
8. Zhang, Y.; Yang, W., Comment on ``Generalized Gradient Approximation Made Simple''. *Physical Review Letters* **1998,** *80* (4), 890-890.
9. Troullier, N.; Martins, J. L., Efficient pseudopotentials for plane-wave calculations. *Physical Review B* **1991,** *43* (3), 1993-2006.
10. Artacho, E.; Sánchez-Portal, D.; Ordejón, P.; García, A.; Soler, J. M., Linear-Scaling ab-initio Calculations for Large and Complex Systems. *physica status solidi (b)* **1999,** *215* (1), 809-817.
11. Even, J.; Pedesseau, L.; Katan, C., Understanding Quantum Confinement of Charge Carriers in Layered 2D Hybrid Perovskites. *ChemPhysChem* **2014,** *15* (17), 3733-3741.
12. Sapori, D.; Kepenekian, M.; Pedesseau, L.; Katan, C.; Even, J., Quantum confinement and dielectric profiles of colloidal nanoplatelets of halide inorganic and hybrid organic–inorganic perovskites. *Nanoscale* **2016,** *8* (12), 6369-6378.
13. Jana, M. K.; Song, R.; Liu, H.; Khanal, D. R.; Janke, S. M.; Zhao, R.; Liu, C.; Valy Vardeny, Z.; Blum, V.; Mitzi, D. B., Organic-to-inorganic structural chirality transfer in a 2D hybrid perovskite and impact on Rashba-Dresselhaus spin-orbit coupling. *Nature Communications* **2020,** *11* (1), 4699.